

ATLAS 1.4 GHz Data Release 2 – II. Properties of the faint polarized sky

C. A. Hales,^{1,2,*†} R. P. Norris,^{2,3} B. M. Gaensler,^{1,3} and E. Middelberg⁴

¹*Sydney Institute for Astronomy, School of Physics, The University of Sydney, NSW 2006, Australia*

²*Australia Telescope National Facility, CSIRO Astronomy and Space Science, P.O. Box 76, Epping, NSW 1710, Australia*

³*ARC Centre of Excellence for All-sky Astrophysics (CAASTRO)*

⁴*Astronomisches Institut, Ruhr-Universität, Universitätsstr. 150, 44801 Bochum, Germany*

Draft version 24 March 2014

ABSTRACT

This is the second of two papers describing the second data release (DR2) of the Australia Telescope Large Area Survey (ATLAS) at 1.4 GHz. In Paper I we detailed our data reduction and analysis procedures, and presented catalogues of components (discrete regions of radio emission) and sources (groups of physically associated radio components). In this paper we present our key observational results. We find that the 1.4 GHz Euclidean normalised differential number counts for ATLAS components exhibit monotonic declines in both total intensity and linear polarization from millijansky levels down to the survey limit of $\sim 100 \mu\text{Jy}$. We discuss the parameter space in which component counts may suitably proxy source counts. We do not detect any components or sources with fractional polarization levels greater than 24%. The ATLAS data are consistent with a lognormal distribution of fractional polarization with median level 4% that is independent of flux density down to total intensity $\sim 10 \text{ mJy}$ and perhaps even 1 mJy. Each of these findings are in contrast to previous studies; we attribute these new results to improved data analysis procedures. We find that polarized emission from 1.4 GHz millijansky sources originates from the jets or lobes of extended sources that are powered by an active galactic nucleus, consistent with previous findings in the literature. We provide estimates for the sky density of linearly polarized components and sources in 1.4 GHz surveys with $\sim 10''$ resolution.

Key words: polarization — radio continuum: galaxies — surveys.

1 INTRODUCTION

A number of studies have reported an anti-correlation between fractional linear polarization and total intensity flux density for extragalactic 1.4 GHz sources; faint sources were found to be more highly polarized (Mesa et al. 2002; Tucci et al. 2004; Taylor et al. 2007; Grant et al. 2010; Subrahmanyam et al. 2010). As a result, the Euclidean-normalised differential number-counts of polarized sources have been observed to flatten at linearly polarized flux densities $L \lesssim 1 \text{ mJy}$ to levels greater than those expected from convolving the known total intensity source counts with plausible distributions for fractional polarization (O’Sullivan et al. 2008). The flattening suggests that faint polarized sources may exhibit more highly ordered magnetic fields than bright sources, or may instead suggest the emergence of an unexpected faint population. The anti-correlation trend for fractional linear polarization is not observed

at higher frequencies ($\geq 4.8 \text{ GHz}$; Sajina et al. 2011; Battye et al. 2011; Massardi et al. 2013).

To investigate possible explanations for the fractional polarization trend seen in previous studies, we have produced the second data release of the Australia Telescope Large Area Survey (ATLAS DR2) as described in Paper I (Hales et al. 2014) of this two paper series. ATLAS DR2 comprises reprocessed and new 1.4 GHz observations with the Australia Telescope Compact Array (ATCA) about the *Chandra* Deep Field-South (CDF-S; Galactic coordinates $l \approx 224^\circ$, $b \approx -55^\circ$; Norris et al. 2006) and European Large Area *Infrared Space Observatory* Survey-South 1 (ELAIS-S1; $l \approx 314^\circ$, $b \approx -73^\circ$; Middelberg et al. 2008) regions in total intensity, linear polarization, and circular polarization. The mosaicked multi-pointing survey areas for ATLAS DR2 are 3.626 deg^2 and 2.766 deg^2 for the CDF-S and ELAIS-S1 regions, respectively, imaged at approximately $12'' \times 6''$ resolution. Typical source detection thresholds are $200 \mu\text{Jy}$ in total intensity and polarization.

In Paper I we presented our data reduction and analysis prescriptions for ATLAS DR2. We presented a catalogue of components (discrete regions of radio emission) comprising 2416 detec-

* E-mail: chales@aoc.nrao.edu

† Current address: National Radio Astronomy Observatory, P.O. Box 0, Socorro, NM 87801, USA; Jansky Fellow of the National Radio Astronomy Observatory.

tions in total intensity and 172 independent detections in linear polarization. No components were detected in circular polarization. We presented a catalogue of 2221 sources (groups of physically associated radio components; grouping scheme based on total intensity properties alone, as described below), of which 130 were found to exhibit linearly polarized emission. We described procedures to account for instrumental and observational effects, including spatial variations in each of image sensitivity, bandwidth smearing with a non-circular beam, and instrumental polarization leakage, clean bias, the division between peak and integrated flux densities for unresolved and resolved components, and noise biases in both total intensity and linear polarization. Analytic correction schemes were developed to account for incompleteness in differential component number counts due to resolution and Eddington biases. We cross-identified and classified sources according to two schemes, summarized as follows.

In the first scheme, described in Section 6.1 of Paper I, we grouped total intensity radio components into sources, associated these with infrared sources from the *Spitzer* Wide-Area Infrared Extragalactic Survey (SWIRE; Lonsdale et al. 2003) and optical sources from Mao et al. (2012), then classified them according to whether their energetics were likely to be driven by an active galactic nucleus (AGN), star formation (SF) within a star-forming galaxy (SFG), or a radio star. Due to the limited angular resolution of the ATLAS data, in Paper I we adopted the term *lobe* to describe both jets and lobes in sources with radio double or triple morphologies. The term *core* was similarly defined in a generic manner to indicate the central component in a radio triple source. Under this terminology, a core does not indicate a compact, flat-spectrum region of emission; restarted AGN jets or lobes may contribute or even dominate the emission observed in the regions we have designated as cores. AGNs were identified using four selection criteria: radio morphologies, 24 μm to 1.4 GHz flux density ratios, mid-infrared colours, and optical spectral characteristics. SFGs and stars were identified solely by their optical spectra. Of the 2221 ATLAS DR2 sources, 1169 were classified as AGNs, 126 as SFGs, and 4 as radio stars. We note that our classification system was biased in favour of AGNs. As a result, the ATLAS DR2 data are in general unsuited for statistical comparisons between star formation and AGN activity.

In the second scheme, described in Section 6.2 of Paper I, we associated linearly polarized components, or polarization upper limits, with total intensity counterparts. In most cases it was possible to match a single linearly polarized component with a single total intensity component, forming a one-to-one match. In other cases this was not possible, due to ambiguities posed by the blending of adjacent components; for example, a polarized component situated mid-way between two closely-separated total intensity components. In these cases, we formed group associations to avoid biasing measurements of fractional polarization. We classified the polarization–total intensity associations according to the following scheme, which we designed to account for differing (de)polarized morphologies (see Paper I for graphical examples):

Type 0 – A one-to-one or group association identified as a lobe of a double or triple radio source. Both lobes of the source are clearly polarized, having linearly polarized flux densities within a factor of 3. (The ratio between lobe total intensity flux densities was found to be within a factor of 3 for all double or triple ATLAS DR2 sources.)

Types 1/2 – A one-to-one or group association identified as a lobe of a double or triple radio source that does not meet the criteria for Type 0. A lobe classified as Type 1 indicates that the ratio of polarized flux densities between lobes is greater than 3. A lobe classified

as Type 2 indicates that the opposing lobe is undetected in polarization and that the polarization ratio may be less than 3, in which case it is possible that more sensitive observations may lead to reclassification as Type 0. Sources with lobes classified as Type 1 exhibit asymmetric depolarization in a manner qualitatively consistent with the Laing-Garrington effect (Laing 1988; Garrington et al. 1988), where one lobe appears more fractionally polarized than the opposite lobe.

Type 3 – A group association representing a source, involving a linearly polarized component situated midway between two total intensity components. It is not clear whether such associations represent two polarized lobes, a polarized lobe adjacent to a depolarized lobe, or a polarized core.

Type 4 – An unclassified one-to-one or group association representing a source.

Type 5 – A one-to-one association clearly identified as the core of a triple radio source (where outer lobes are clearly distinct from the core).

Type 6 – A source comprising two Type 0 associations, or a group association representing a non-depolarized double or triple radio source where blended total intensity and linear polarization components have prevented clear subdivision into two Type 0 associations.

Type 7 – A source comprising one or two Type 1 associations.

Type 8 – A source comprising one Type 2 association.

Type 9 – An unpolarized component or source.

In this work (Paper II) we present the key observational results from ATLAS DR2, with particular focus on the nature of faint polarized sources. This paper is organised as follows. In Section 2 we present the ATLAS DR2 source diagnostics resulting from infrared and optical cross-identifications and classifications, diagnostics resulting from polarization–total intensity cross-identifications and classifications, differential component number-counts, and our model for the distribution of fractional polarization. In Section 3 we compare the ATLAS DR2 differential counts in both total intensity and linear polarization to those from other 1.4 GHz surveys, and discuss asymmetric depolarization of classical double radio sources. We present our conclusions in Section 4. This paper follows the notation introduced in Paper I. We typically denote flux density by S , but split into I for total intensity and L for linearly polarized flux density when needed for clarity.

2 RESULTS

2.1 Multiwavelength Cross-Identifications and Classifications

In the following sections we present diagnostics of ATLAS DR2 sources resulting from the infrared and optical cross-identification and classification schemes described in Section 6.1 of Paper I (summarised in Section 1 of this work). We focus on three parameter spaces formed by comparing flux densities between different wavelength bands: radio to mid-infrared, mid-infrared colours, and radio to far-infrared.

2.1.1 Radio vs Mid-Infrared

In Fig. 1 we compare the total intensity 1.4 GHz radio to 3.6 μm mid-infrared flux densities for all 2221 ATLAS DR2 sources, taking into account infrared upper bounds for the 298 radio sources without detected infrared counterparts. The bottom-right panel of

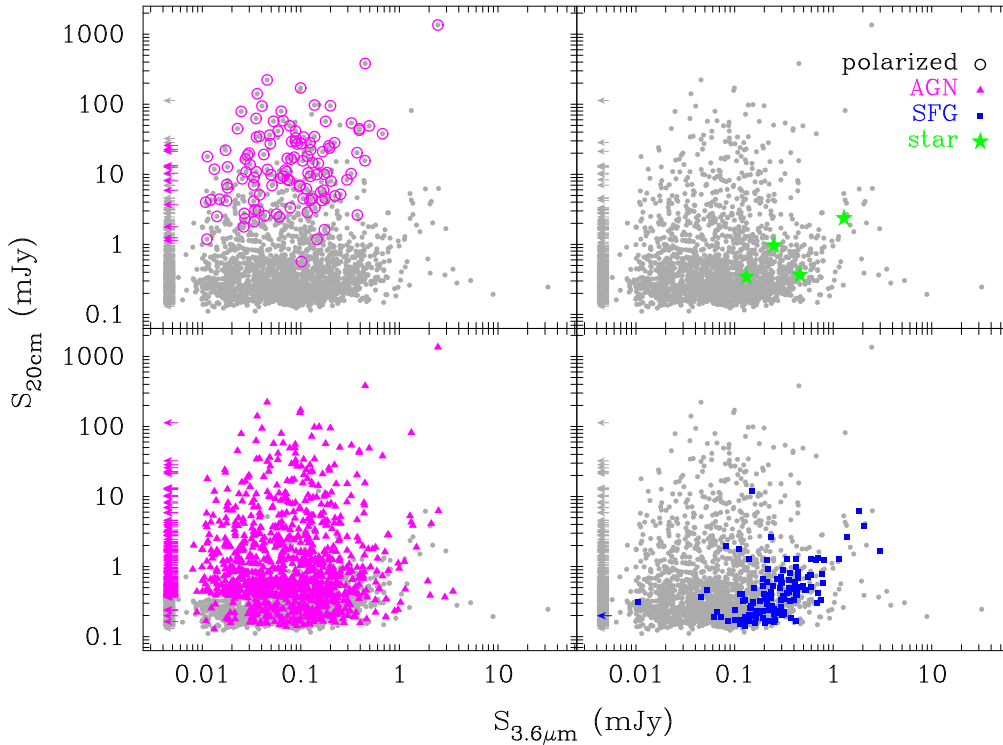


Figure 1. Comparison of radio to mid-infrared flux densities for all ATLAS DR2 sources, as indicated by the grey points and grey upper bounds in each panel. For clarity, multiple panels are used to focus on different source populations. In each panel, the highlighted population includes those sources represented by upper bounds. The bottom-left panel highlights all sources classified as AGNs in ATLAS DR2. The bottom-right panel highlights all sources classified as SFGs. The top-left panel highlights all sources exhibiting linearly polarized emission, where the colour of the highlighted points and upper bounds indicates whether the source is an AGN, SFG, or star (i.e. they are all AGNs). The top-right panel highlights all sources identified as stars.

Fig. 1 indicates that the ATLAS sources classified as stars or SFGs typically exhibit radio flux densities $\lesssim 1$ mJy. The paucity of ATLAS sources with $S_{3.6\mu\text{m}} \lesssim 0.1$ mJy and star or SFG classifications likely represents a selection bias, in which only those sources with relatively bright optical counterparts could be classified spectroscopically. The top-left panel highlights all 130 polarized ATLAS sources, 12 of which are represented by upper bounds. The paucity of polarized sources with $S_{20\text{cm}} \lesssim 1$ mJy is due to the limited sensitivity of our linear polarization data; fractional polarization trends will be presented in Section 2.2.

2.1.2 Mid-Infrared Colours

In Fig. 2 we present mid-infrared colour-colour diagrams in which the IRAC flux density ratios $S_{8.0\mu\text{m}}/S_{4.5\mu\text{m}}$ and $S_{5.8\mu\text{m}}/S_{3.6\mu\text{m}}$ have been compared for ATLAS DR2 sources. Of the 2221 ATLAS sources, 988 were detected in all four IRAC bands, while 935 were detected in only 2 or 3 bands; the remaining 298 sources were not detected in any band, and have not been shown in Fig. 2. Regarding the 130 polarized ATLAS sources, 55 were detected in all four IRAC bands, 63 were detected in only 2 or 3 bands, and 12 were not detected in any IRAC band; thus 118 polarized sources are indicated in Fig. 2.

The dotted lines in each panel of Fig. 2 represent the divisions identified through simulations by Sajina, Lacy, & Scott (2005). By considering the effects of redshift evolution on the observed mid-infrared colours of three general source classes with spectral characteristics dominated by old-population (10 Gyr) starlight, polycyclic aromatic hydrocarbon (PAH) emission, or a power-law con-

tinuum, Sajina, Lacy, & Scott (2005) identified four regions that could be used to preferentially select different source classes at different redshifts within the $z = 0 - 2$ range simulated. Region 1 was found to preferentially select sources with spectra dominated by continuum emission, likely produced by dust tori associated with AGNs (Pier & Krolik 1993; Nenkova et al. 2008), over the full redshift range. Region 2 was found to preferentially select PAH-dominated sources, indicative of intense star formation, over the full redshift range. Region 3 was found to preferentially select sources with spectra dominated by direct stellar light, but only for sources with $z \lesssim 0.4$. For increasing redshifts, region 3 was found to comprise a mixture of stellar- and PAH-dominated sources as the latter migrated from region 2. However, beyond $z \gtrsim 1.6$, region 3 was found to be largely void of sources following the migrations of both stellar- and PAH-dominated sources towards region 4. Region 4 was found to be largely void of sources for $z \lesssim 0.4$. For increasing redshifts, PAH-dominated sources were found to migrate from region 2 into region 4. For $z \gtrsim 0.9$, stellar-dominated sources from region 3 were also found to migrate into region 4. Sajina, Lacy, & Scott (2005) found that at all redshifts, sources dominated by PAH emission were located slightly within the boundaries of region 1. In order to classify as AGNs only those sources most likely to be such in Fig. 2, we constructed the restricted locus indicated by the dashed lines; we label this region 1R. In Paper I we defined this locus (following Padovani et al. 2011) as the union of $\log_{10}[S_{8.0\mu\text{m}}/S_{4.5\mu\text{m}}] > 0$, $\log_{10}[S_{5.8\mu\text{m}}/S_{3.6\mu\text{m}}] > 0$, and $\log_{10}[S_{8.0\mu\text{m}}/S_{4.5\mu\text{m}}] < 11 \log_{10}[S_{5.8\mu\text{m}}/S_{3.6\mu\text{m}}]/9 + 0.3$. Continuum-dominated sources are expected to exhibit power-law spectra, given by the dot-dashed locus in each panel. As noted by

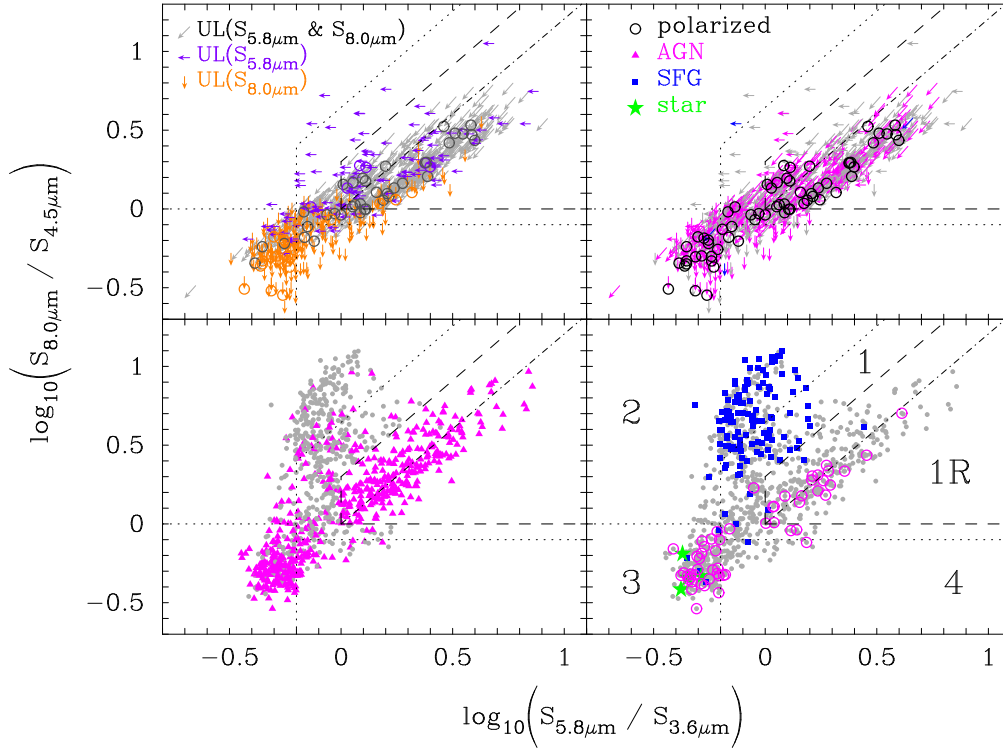


Figure 2. Mid-infrared colour-colour diagrams in which ATLAS DR2 sources with an infrared counterpart detected in at least two IRAC bands are displayed (84% of all ATLAS DR2 sources). Radio sources with counterparts detected in all four IRAC bands are displayed in the lower panels. Those with infrared counterparts detected in only two or three IRAC bands are displayed in the upper panels. Data are replicated within the panels in each row to highlight different source populations. In each panel except the top-left, grey points or grey upper bounds indicate unclassified sources. The bottom-left panel highlights all sources classified as AGNs. The bottom-right panel highlights all sources classified as SFGs, stars, and those exhibiting polarized emission; each polarized source has been coloured according to its AGN/SFG/star classification. The top-right panel displays upper bounds, colour-coded according to their AGN/SFG/star classification. The 63 polarized sources indicated within this panel are all classified as AGNs, but shown black in this panel for visual contrast. The top-left panel shows upper bounds, colour-coded according to the non-detected bands. The dotted lines in each panel outline the four regions identified by Sajina, Lacy, & Scott (2005), as described in Section 2.1.2. The dashed lines outlining region 1R indicate the restricted locus adopted in this parameter space for classifying AGNs, as described in Section 2.1.2. The dot-dashed line in each panel indicates the locus of sources exhibiting red power-law spectra over the four IRAC bands.

Sajina, Lacy, & Scott (2005), the spectra of continuum-dominated sources are only expected to exhibit blue IRAC colours for largely unobscured AGNs, in cases for which their rest-frame optical wavelengths are redshifted into the mid-infrared band for sources at $z > 2$. Thus the ATLAS sources with blue IRAC colours in Fig. 2 are unlikely to be represented by continuum-dominated sources as defined by Sajina, Lacy, & Scott (2005). However, this does not imply that a source observed with blue IRAC colours at $z < 2$ cannot be an AGN, because sources with mid-infrared spectra dominated by old stellar light may yet exhibit stronger signs of AGN activity at other wavelengths.

The bottom-left panel of Fig. 2 indicates that ATLAS sources classified as AGNs are predominantly located in regions 1R and 3. The sources classified as AGNs in region 2 perhaps suggest combinations of star formation and AGN activity, or perhaps misclassifications due to the largely statistical nature of our classification system. The upper bounds classified as AGNs in the top-right panel are consistent with the observed distribution of AGNs presented in the bottom-left panel. These upper bounds suggest that additional AGNs are situated in region 4, though likely in proportion with the additional AGNs remaining undetected in regions 1 and 3. The bottom-right panel indicates that ATLAS sources classified as SFGs are predominantly located in region 2, as well as between the boundaries of regions 1 and 1R, as expected. A small num-

ber of ATLAS sources classified as SFGs are located in regions 1R and 3, consistent with the migratory paths of PAH-dominated sources. The upper bounds classified as SFGs in the top-right panel are consistent with the majority of SFGs being located in region 2. All 4 ATLAS sources classified as stars are located in region 3. The polarized ATLAS sources detected in all four IRAC bands follow the distribution of AGNs, situated predominantly in regions 1 and 3 in almost equal proportions. The upper bounds for polarized sources presented in the top-right panel are consistent with this finding. The lack of polarized sources in region 2 suggests that the polarized ATLAS sources observed in region 3 are unlikely to be SFGs with rest-frame colours located in region 2 (i.e. if SFGs are migrating from region 2 to region 3 with redshift, then a trail of sources would be expected). Instead, we find two concentrations of polarized ATLAS sources, highly coincident with the regions of parameter space identified by Sajina, Lacy, & Scott (2005) in which starlight- and continuum-dominated sources were preferentially located.

Thus we find that the radio emission from polarized ATLAS sources is most likely powered by AGNs, where the active nuclei are embedded within host galaxies with mid-infrared spectra dominated by old-population stellar light (blue IRAC colours) or continuum likely produced by dusty tori (red IRAC colours). This finding is in general agreement with the results from the

ELAIS-North 1 (ELAIS-N1) region presented by both Taylor et al. (2007) and Banfield et al. (2011), but with the following two notable exceptions. First, both these works identified radio sources (both polarized and unpolarized) that were concentrated in region 3 about $\log_{10}(S_{5.8\,\mu\text{m}}/S_{3.6\,\mu\text{m}}) = -0.6$, $\log_{10}(S_{8.0\,\mu\text{m}}/S_{4.5\,\mu\text{m}}) = -0.7$, well beyond the parameter space typically occupied by the three generic source classes investigated by Sajina, Lacy, & Scott (2005). Taylor et al. (2007) reported that these sources were associated with elliptical galaxies dominated by old-population starlight. However, Fig. 11 from Sajina, Lacy, & Scott (2005) indicates that these sources are located within a region of parameter space occupied by individual stars. It is not clear why the IRAC colours of so many of the radio sources presented by Taylor et al. (2007) and Banfield et al. (2011) were found to occupy this region of parameter space, though it is possible that their selection of isophotal flux densities for unresolved infrared sources may have biased their colour ratios (aperture values are more appropriate for point sources). And second, unlike these previous works, we do not find any polarized ATLAS sources in which the radio emission is likely to be powered by star formation (i.e. we do not see any polarized sources in region 2; cf. Banfield et al. 2011); we cannot conclude that any polarized sources have infrared colours suggestive of significant PAH emission (cf. Taylor et al. 2007). The fractional polarization properties of ATLAS AGNs and SFGs are described in Section 2.2 and modelled in Section 2.4.

2.1.3 Radio vs Far-Infrared

In Fig. 3 we compare the total intensity 1.4 GHz radio to 24 μm infrared flux densities for all ATLAS DR2 sources, taking into account infrared upper bounds for all radio sources without detected infrared counterparts. As noted in Paper I, we use 24 μm flux density as a proxy for far-infrared (FIR) flux density. The bottom-left panel indicates that ATLAS sources classified as AGNs are prevalent both away from and on the FIR-radio correlation (FRC). The presence of a substantial number of AGNs below the dashed line demonstrates the value of using multiple diagnostic criteria to classify sources; only sources above the dashed line have been classified as AGNs using the radio to far-infrared diagnostic. The bottom-right panel indicates that, as expected, ATLAS sources classified as SFGs typically cluster along the FRC and have radio flux densities $\lesssim 1$ mJy. However, a small number of sources classified as SFGs (and stars) are observed with upper bounds clearly located within the AGN parameter space. The top-left panel highlights all 130 polarized ATLAS sources, indicating that each of these was classified as an AGN. No polarized stars or SFGs were detected in our data.

2.2 Polarization Cross-Identifications and Classifications

We now present diagnostics of components, groups, and sources in ATLAS DR2, resulting from the linear polarization–total intensity cross-identification and classification procedures described in Section 6.2 of Paper I (summarised in Section 1 of this work). In this section we focus on a number of parameter spaces in which we detail relationships between the polarized flux densities, fractional polarizations, classifications, and angular sizes of sources and their constituents.

2.2.1 Components, Groups, and Sources

In Fig. 4 we plot the polarized flux densities and fractional polarizations for all ATLAS DR2 components, groups, and sources versus their total intensity flux densities, taking into account polarization upper limits. The fractional polarization uncertainties displayed in the lower-left panel were estimated following standard error propagation as

$$\sigma_{\Pi} \approx \Pi \sqrt{\left(\frac{\sigma_I}{I}\right)^2 + \left(\frac{\sigma_P}{P}\right)^2}. \quad (1)$$

Fig. 4 shows that the polarization upper limits for components and sources are distributed almost identically, the reason being that the majority of unpolarized sources comprise a single component (relevant statistics are detailed toward the end of this section). Regarding polarization detections, we find that all components, groups, and sources exhibit $\Pi < 24\%$. This finding is in contrast to the data from other 1.4 GHz polarization surveys. Shi et al. (2010) found that 1% (381/38454) of polarized sources in the NRAO VLA Sky Survey (NVSS) exhibited $\Pi \geq 30\%$. Taylor et al. (2007) and Grant et al. (2010) found that 10% (8/83) and 7% (10/136) of polarized sources in the ELAIS-N1 field exhibited $\Pi \geq 30\%$, respectively. Subrahmanyan et al. (2010) found that 10% (84/869) of polarized sources throughout the two Australia Telescope Low-Brightness Survey (ATLAS) fields exhibited $\Pi \geq 30\%$. If a population of extragalactic sources with high 1.4 GHz fractional polarizations were to exist, then it would be unexpected for such sources to be detected in the surveys above [with $\sim 50''$ full-width at half-maximum (FWHM) beam sizes] yet undetected in this work (with $\sim 10''$ FWHM beam size), because the former are more susceptible to both beam and bandwidth depolarization. Instead, we attribute the lack of ATLAS sources with $\Pi > 30\%$ to our careful treatment of local (rather than global) root mean square (rms) noise estimates, in particular to our employment of BLOBCAT’s flood-fill technique for extracting polarized flux densities (see Hales et al. 2012b for details regarding biases introduced through Gaussian fitting), and to our statistical classifications of unresolved and resolved components. We found through testing that components with abnormally high levels of fractional polarization (up to and even beyond 100%) could be obtained if the features above were not taken into account.

2.2.2 Multiwavelength Classifications

In Fig. 5 we plot the polarized flux densities and fractional polarizations for all ATLAS DR2 sources only, indicating their infrared/optical classifications. Panels in the left column highlight polarized sources with infrared counterparts detected in all four IRAC bands, or otherwise. We split those detected in all four bands into sources located within or just beyond region 3 in the lower-right panel of Fig. 2 [i.e. polarized sources with $\log_{10}(S_{5.8\,\mu\text{m}}/S_{3.6\,\mu\text{m}}) < -0.1$] and those located within or just beyond region 1R [i.e. $\log_{10}(S_{5.8\,\mu\text{m}}/S_{3.6\,\mu\text{m}}) > -0.1$]. We find no clear distinction between the fractional polarization properties of sources with blue (region 3) or red (region 1R) mid-infrared colours. It is possible that the region 3 polarized sources exhibit a larger dispersion in fractional polarization than the region 1R polarized sources (compare range of observed fractional polarizations in lower-left panel of Fig. 5), though given our sample size this marginal effect may be attributed to sampling variance. Using data from Grant et al. (2010), Banfield et al. (2011) found that polarized sources in region 3 were more highly polarized than those in region 1R; the ATLAS data do not support this result. The dis-

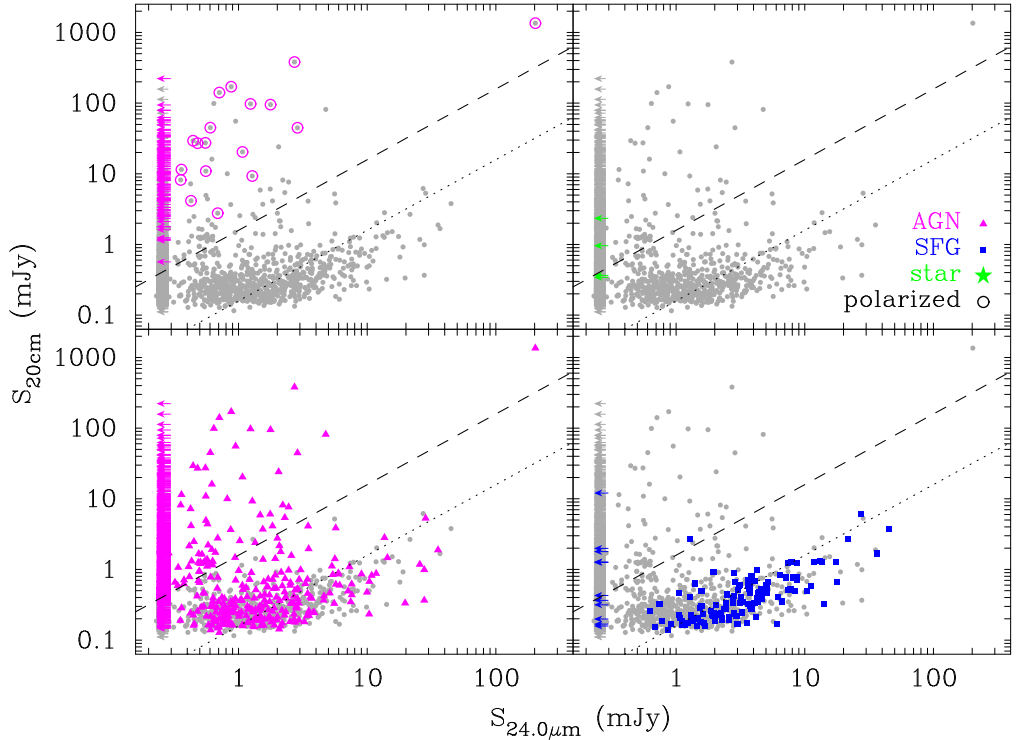


Figure 3. Comparison of radio to far-infrared flux densities for all ATLAS DR2 sources observed at $24\mu\text{m}$, as indicated by the grey points and grey upper bounds in each panel. For clarity, multiple panels are used to focus on different source populations. The dotted line in each panel indicates the FRC, defined by Appleton et al. (2004) as $q_{24} = 0.8$. The dashed lines indicate our adopted criteria for classifying AGNs, based on radio flux densities 10 times greater than the FRC. In each panel, the highlighted population includes those sources represented by upper bounds. The bottom-left panel highlights all sources classified as AGNs in ATLAS DR2. The bottom-right and top-right panels highlight all sources classified as SFGs and stars, respectively. The top-left panel highlights all sources exhibiting linearly polarized emission, where the colours of the highlighted points and upper bounds indicate whether a source has been classified as an AGN, SFG, or star (i.e. they are all AGNs).

tributions of upper limits presented in the right-column panels of Fig. 5 indicate that all sources with $\Pi < 1\%$ have been classified as AGNs. The fractional polarization upper limits for sources classified as SFGs are not particularly restrictive, as their total intensity flux densities are typically $\lesssim 1$ mJy. Characteristic Π levels for the sub-millijansky SFG population are $\lesssim 60\%$.

2.2.3 Distribution of Fractional Linear Polarization

Focusing on the lower-left panel of Fig. 5, we note that a general observational consequence of the rising distribution of fractional polarization upper limits with decreasing total intensity flux density is that the mean or median fractional polarization of *detected* polarized sources will always *appear* to increase with decreasing flux density. This increase represents a selection bias; it is not possible to detect low levels of fractional polarization for the faintest total intensity sources. Any changes to the underlying distribution of fractional polarization with decreasing total intensity flux density will be masked, and thus dominated, by this selection bias. Therefore, it is not possible to investigate the distribution of fractional polarization at faint flux densities without accounting for polarization non-detections. Recently, 1.4 GHz polarimetric studies of the ELAIS-N1 field (Taylor et al. 2007; Grant et al. 2010) and ATLAS fields (Subrahmanyan et al. 2010) concluded that their observational data demonstrated an anti-correlation between fractional polarization and total intensity flux density. These studies found that sources with $I \lesssim 10$ mJy were more highly polarized than stronger sources. However, Subrahmanyan et al. (2010)

did not account for polarization upper limits, leading to their misinterpretation of selection bias as an indication of true anti-correlation. Taylor et al. (2007) accounted for selection bias using Monte Carlo analysis, effectively incorporating polarization upper limits. Grant et al. (2010) accounted for selection bias by comparing samples of sources in bins of polarized flux density rather than total flux density, at sufficient polarized flux densities to neglect upper limits. However, the findings of increased fractional polarization at faint total flux densities by Taylor et al. (2007) and Grant et al. (2010) appear to be reliant on the increasing number of sources observed with $\Pi > 30\%$ at these faint levels. For example, both studies reported extreme sources with $\Pi > 60\%$, but only at faint total intensities. Both Taylor et al. (2007) and Grant et al. (2010) found that $\sim 13\%$ of polarized sources with linearly polarized flux densities $L < 2$ mJy (i.e. a significant proportion of these sources) exhibited $\Pi > 30\%$, while no sources with such high levels of fractional polarization were found for $L > 2$ mJy. As described earlier, the $\Pi > 30\%$ sources (and perhaps many with lower Π) are likely to reflect rms noise estimation and source extraction errors. The analytic form assumed by Taylor et al. (2007) for the distribution of fractional polarization (which will be described in Section 2.4) may have also contributed to their conclusion regarding increased fractional polarization; spurious conclusions may be obtained if the observed fractional polarization data do not follow the assumed analytic form of the fit. The arguments above suggest that existing evidence for an anti-correlation between fractional polarization and total flux density may not be robust.

Similar to the studies above, earlier works by Mesa et al.

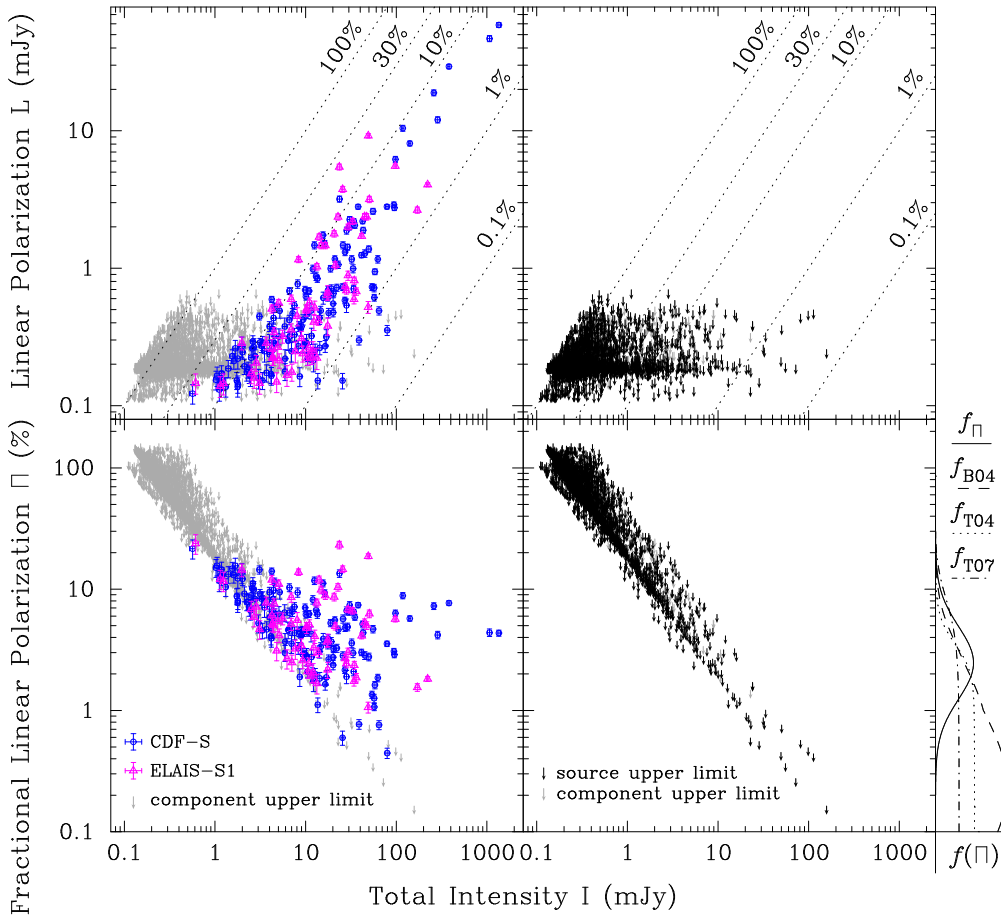


Figure 4. Linearly polarized flux density (upper panels) and corresponding fractional linear polarization (lower panels) versus total intensity flux density for all ATLAS DR2 components, groups and sources. Dotted lines in the upper panels indicate fractional polarizations of 0.1%, 1%, 10%, 30%, and 100%. Upper limits for unpolarized components are shown in the left panels and replicated in the right panels. Upper limits for unpolarized sources are shown only in the right panels. Polarization detections are shown only in the left panels. Polarized components (i.e. one-to-one associations), groups, and sources, which are not differentiated in this Figure, are indicated in the left panels and colour-coded according to their respective ATLAS field. The curves adjacent to the lower-right panel replicate the fractional polarization distributions presented in Fig. 14 (see Section 2.4).

(2002) and Tucci et al. (2004) concluded that NVSS (Condon et al. 1998) sources exhibited an anti-correlation between fractional linear polarization and total intensity flux density. These analyses in effect incorporated polarization upper bounds (though not upper limits; see Kashyap et al. 2010) because Condon et al. (1998) recorded a linearly polarized flux density for each NVSS source, regardless of the statistical significance of the polarization measurement. To determine the significance of their findings and thus form a conclusion regarding evidence for anti-correlation, which we use to justify our own fractional polarization model presented in Section 2.4, we need to examine their works in more detail.

Mesa et al. (2002) and Tucci et al. (2004) presented fractional polarization distributions for steep- and flat/inverted-spectrum NVSS sources in four flux density intervals: 100 – 200, 200 – 400, 400 – 800, and > 800 mJy. Their distributions are remarkably consistent for $\Pi > 1\%$, exhibiting a log-normal form with approximately equal dispersion and a peak at $\sim 2.5\%$. A separate component with a peak at $\sim 0.2\%$ is also present in each distribution, representing sources with polarization dominated by instrumental leakage. We observe that the dispersions of their distributions broaden with increasing flux density, solely due to broadening at $\Pi < 1\%$. Mesa et al. (2002) found that the median fractional polarization was larger for the 100 – 200 mJy data than for

the > 800 mJy data, for both steep- and flat-spectrum sources. Tucci et al. (2004) found the same result but for steep-spectrum sources only. These results were essentially based on the lack of sources with $\Pi < 0.1\%$ in the 100 – 200 mJy data when compared with the increased presence of such sources at higher flux densities; a proportional increase in the number of sources with $\Pi > 1\%$ for decreasing flux density was not observed. However, the presence of sources with $\Pi < 0.1\%$ (i.e. less than the typical leakage level of $\sim 0.2\%$), and more generally the slight changes in distribution shape observed for $\Pi < 1\%$ between different flux density intervals, may be more appropriately explained by the influence of noise on polarized flux densities rather than by variation in the underlying distribution of fractional polarization. To demonstrate, we first note that the expectation value of L for an unpolarized NVSS source is given by the mean of a Rayleigh distribution (i.e. a Ricean distribution with no underlying polarized signal), which is $\sqrt{\pi}\sigma_{Q,U}/2 \approx 0.36$ mJy for $\sigma_{Q,U} \approx 0.29$ mJy. This value is also characteristic of the expected observed polarized flux density for a source with true underlying polarized signal $L_0 \lesssim \sigma_{Q,U}$ (e.g. see the upper panel of Fig. 1 from Hales et al. 2012a). Thus, a tail of sources with true polarization $L_0 \lesssim 0.29$ mJy will appear in the fractional polarization distribution at $\Pi \gtrsim 0.18\%$ for total intensity sources with $I < 200$ mJy, and at $\Pi \lesssim 0.05\%$ for $I > 800$ mJy.

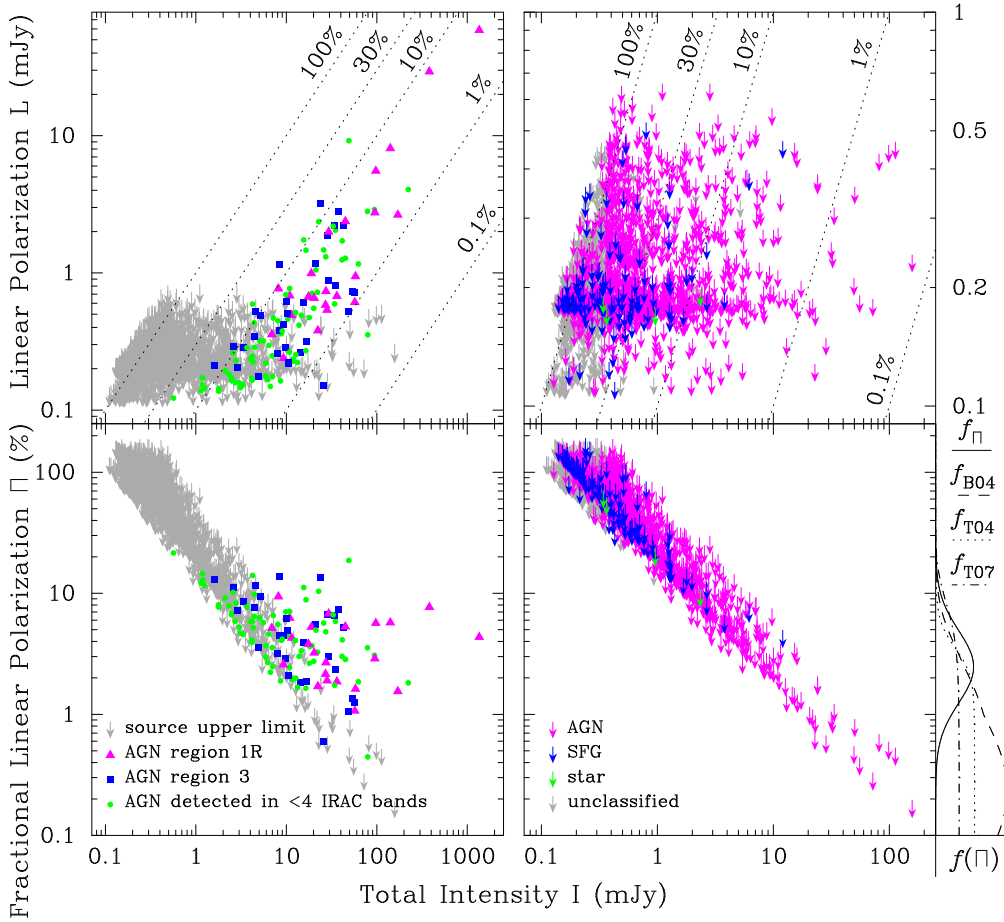


Figure 5. Linearly polarized flux density (upper panels) and corresponding fractional linear polarization (lower panels) versus total intensity flux density for all ATLAS DR2 sources. The panel layout is similar to Fig. 4; the legends are independent for each column. Panels in the left column highlight polarized sources with infrared counterparts that exhibit blue [sources located within or just beyond region 3 with $\log_{10}(S_{5.8\mu\text{m}}/S_{3.6\mu\text{m}}) < -0.1$] or red [sources located within or just beyond region 1R with $\log_{10}(S_{5.8\mu\text{m}}/S_{3.6\mu\text{m}}) > -0.1$] mid-infrared colours according to the colour-colour diagram in the lower-right panel of Fig. 2. Note that all polarized ATLAS DR2 sources have been classified as AGNs. For comparison, upper limits for all unpolarized sources are presented in the background. Panels in the right column highlight AGN/SFG/star classifications for these unpolarized sources. Note that x-axis scaling differs between columns, and that y-axis scaling differs between the two upper panels.

These estimates are consistent with the distributions presented by Mesa et al. (2002) and Tucci et al. (2004); a tail of sources with $\Pi < 0.1\%$ was observed for the > 800 mJy data but not for the $100 - 200$ mJy data. We therefore conclude that the results presented by Mesa et al. (2002) and Tucci et al. (2004) do not demonstrate a statistically significant anti-correlation between fractional linear polarization and total intensity flux density. Furthermore, we note that the fractional polarization distributions presented in these works are likely to overestimate the population of sources with $\Pi < 1\%$, even for the $100 - 200$ mJy data, for the following two reasons. First, all catalogued NVSS measurements of polarized flux density were debiased using a modified version of the expectation value for a Ricean distribution (Condon et al. 1998). This debiasing scheme is known to impart a significant overcorrection (i.e. negative bias) at low SNR (e.g. see Simmons & Stewart 1985; the relevant scheme is labelled in reference to its application by Serkowski 1958). Thus measurements of fractional polarization obtained using the NVSS catalogue are likely to be negatively biased. And second, raw polarization measurements for NVSS sources were obtained by interpolation at the total intensity centre position. Therefore, polarized flux densities were underestimated for each source in which the spatial peak of polarized emission was located in an

adjacent pixel to the total intensity peak. Both of these effects could have been largely mitigated by obtaining polarization upper limits for sources, rather than upper bounds.

Returning to the lower-left panel of Fig. 5, we find that the maximum level of fractional polarization exhibited by ATLAS sources does not appear to be correlated with total intensity flux density. The maximum level appears to be limited to $\Pi \lesssim 20\%$ for $I \gtrsim 1$ mJy, which becomes a strict limit for $I > 4$ mJy when accounting for the presence of all upper limits. Furthermore, we find $\Pi \gtrsim 0.4\%$ for sources with $I \gtrsim 10$ mJy, where sources exhibiting higher levels of fractional polarization significantly outnumber those potentially exhibiting $\Pi < 0.4\%$ as indicated by the upper limits.

2.2.4 Polarization Classifications

In Paper I we found that 138 of the total 172 catalogued linearly polarized components exhibited a clear one-to-one match with individual total intensity components. The remaining 34 polarized components required grouping in order to be associated with total intensity counterparts. Of the one-to-one associations, we classified 58 as Type 0, 4 as Type 1, 25 as Type 2, 48 as Type 4, and 3 as Type

5. All 3 sources containing Type 5 core associations were found to exhibit unpolarized lobes. Of the group associations comprising a total of 34 polarized components, 2 groups were classified as Type 0, 14 as Type 3, 1 as Type 4, and 8 as Type 6. There were 29 sources classified as Type 6, 2 as Type 7, and 25 as Type 8. These classifications are catalogued in Appendix B of Paper I.

In Fig. 6 we indicate the polarization–total intensity classifications for all polarized ATLAS DR2 components, groups, and sources. In the lower-left panel we plot the levels of fractional polarization exhibited by classical double or triple radio sources (Types 6–8) and their individual lobes (Types 0–2, respectively). We find that sources classified as Type 6, which comprise pairs of roughly equally polarized Type 0 lobes, are located throughout most of the populated parameter space. We find that Type 7 sources, which comprise pairs of Type 1 lobes where one is clearly less polarized than the other, appear to occupy the same parameter space populated by Type 6 sources. A selection bias against identifying Type 0/1 lobes, and thus Type 6/7 sources, is present within the diagonal region of parameter space populated by polarization upper limits (for visual clarity these limits are not shown in Fig. 6; see Fig. 4). Type 2 lobes and their parent Type 8 sources, which represent ambiguous cases in which it is not possible to differentiate between Types 0/1 or 6/7, are largely confined to this diagonal region. Given the observed prevalence of Type 6 sources compared with Type 7, it seems likely that more sensitive observations would result in a majority of Type 8 sources being reclassified as Type 6. From the lower-right panel of Fig. 6 we find that sources classified as Type 3, which exhibit a single polarized component situated midway between two total intensity components, appear to populate the same region of parameter space occupied by Type 8 sources. Similarly, associations classified as Type 5, which represent cores of triple radio sources, as well as the remaining unclassified sources denoted by Type 4, also appear to be concentrated within the diagonal region of parameter space populated by upper limits. We note that many of the Type 4 associations are likely to represent individual Type 0 or Type 1 lobes of as-yet unassociated multi-component sources, having been erroneously assigned to single-component sources in our catalogue (note Section 6.1 of Paper I; statistics regarding polarized multi-component sources are presented below). We find that Type 5 associations occupy a parameter space consistent with Type 6 and Type 7 sources. As the latter represent average polarization properties for dual-lobed radio sources, it is possible that Type 5 associations also represent dual-lobed structures but with small angular sizes, such as compact steep-spectrum (CSS) sources (O’Dea 1998). Curiously, we found that each of the 3 sources with Type 5 cores was found to exhibit unpolarized outer radio lobes. It is possible that the Type 5 cores represent restarted AGN activity and that the outer lobes are unpolarized because any large-scale magnetic fields within them have dissipated over time since their production during an earlier distinct phase of AGN activity. For example, we may be seeing sources similar to the double-double radio galaxy J1835+620 (Lara et al. 1999), though at an earlier stage of evolution where the inner lobes have not yet separated into two separate lobes (note that fractional polarization levels for the inner lobes of J1835+620 are higher than for the outer lobes).

2.2.5 Angular Sizes

In Fig. 7 we plot polarized flux density and fractional polarization versus largest angular size (LAS) for all polarized ATLAS DR2 sources, highlighted according to morphology and infrared colour.

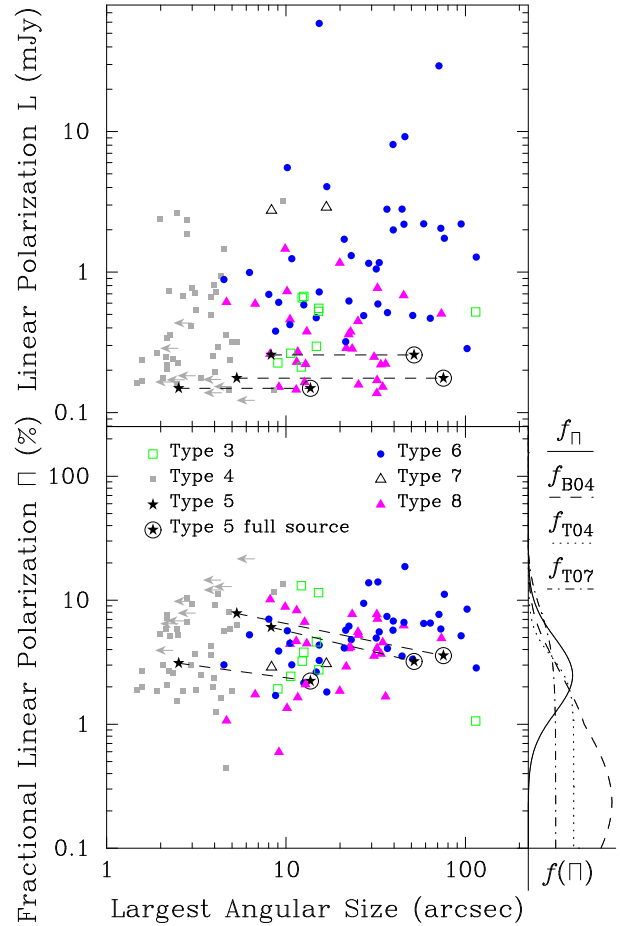


Figure 9. Reproduction of data from Fig. 7, highlighted here according to the classification scheme presented in Section 6.2 of Paper I (summarised in Section 1 of this work). Note that under this scheme, only Types 3, 4, 6, 7, or 8 may represent sources. Additional data points are displayed for Type 5 one-to-one associations (which represent polarized cores within classical triple morphologies) with abscissae given by their deconvolved angular sizes, and for their parent sources (which include outer lobes) with abscissae given by their LASs.

The LAS for a single-component source is given by its total intensity deconvolved angular size or size upper limit, while the LAS for a multi-component source is given by the maximum angular separation between its constituent total intensity components. For visual clarity we plot sources with polarization upper limits separately in Fig. 8, also highlighted according to morphology and infrared colour. Note that the apparent anti-correlations between fractional polarization upper limits and angular size upper limits for single-component sources throughout Fig. 8 are spurious; the restrictiveness of both types of upper limits are intrinsically anti-correlated with total intensity flux density. In Fig. 9 we again plot polarized flux density and fractional polarization versus LAS for all polarized sources, but now highlighted according to the polarization–total intensity classification scheme from Section 6.2 of Paper I. For reference, we note that $1''$ subtends a linear scale of 1.8, 3.3, 6.1, 8.0, and 8.5 kpc at redshifts 0.1, 0.2, 0.5, 1.0, and 2.0, respectively (Wright 2006), assuming a Λ CDM cosmology with parameters $H_0 = 71 \text{ km s}^{-1} \text{ Mpc}^{-1}$, $\Omega_m = 0.27$, and $\Omega_\Lambda = 0.73$. Following an evolutionary relationship for galaxy sizes given by

$$\text{diameter (linear scale)} \propto H_0^{-1} [\Omega_m (1+z)^3 + \Omega_\Lambda]^{-\frac{1}{2}}, \quad (2)$$

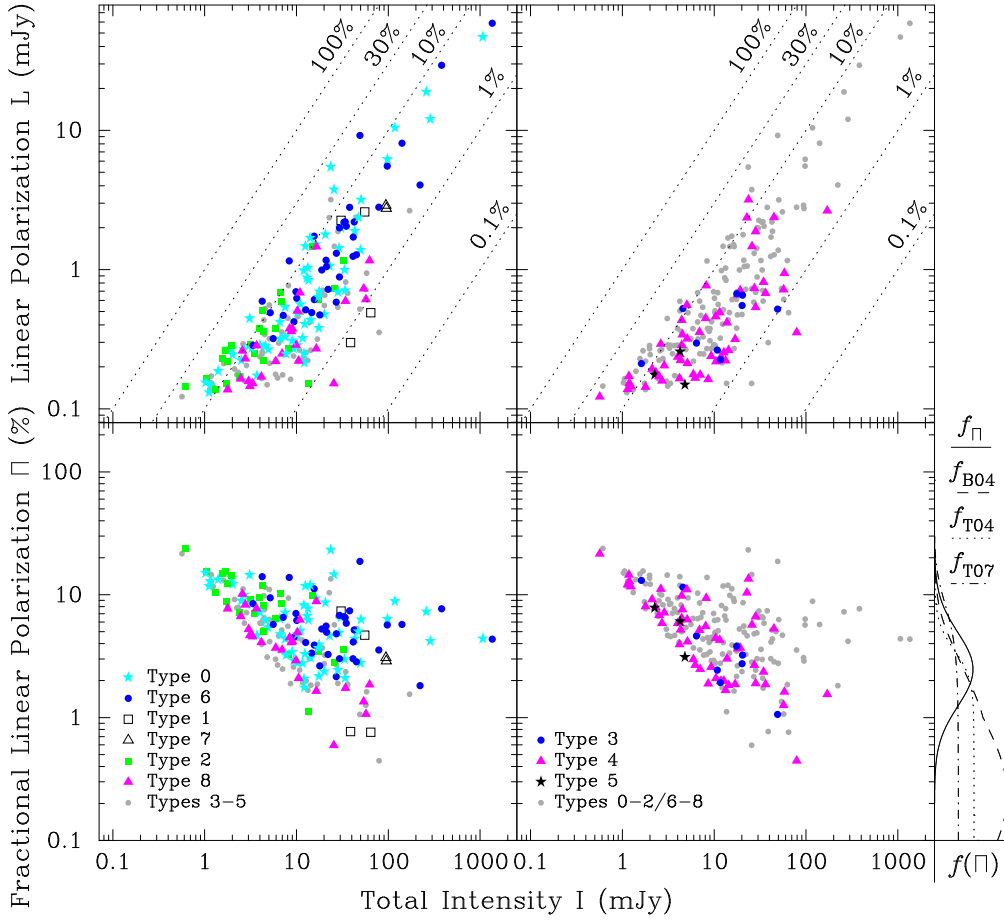


Figure 6. Polarized ATLAS DR2 components, groups and sources from the left column of Fig. 4, highlighted here according to the classification scheme presented in Section 6.2 of Paper I (summarised in Section 1 of this work). The legends are independent for each column. Note that only Types 3, 4, 6, 7, or 8 may represent sources.

and assuming that a typical galaxy has size ~ 20 kpc at $z = 0$ (e.g. Ferguson et al. 2004), the corresponding sizes of typical galaxies at the redshifts above are approximately¹ 19, 18, 16, 12, and 7 kpc, respectively, or $10''$, $5''$, $2''$, $1''$, and $0''$, respectively. We summarise our findings from Figs. 7–9 as follows.

Of the 130 (2091) polarized (unpolarized) sources catalogued in ATLAS DR2 and presented in Fig. 7 (Fig. 8), 81 (74) comprise multiple components in total intensity, 40 (140) comprise a single resolved component in total intensity, and 9 (1877) comprise a single unresolved component in total intensity. We note that while components observed in linear polarization in ATLAS DR2 are typically unresolved (only 29/172 or 17% of polarized components are resolved; see Section 5 of Paper I), 121/130 or 93% of sources exhibiting polarized emission are resolved in total intensity. These statistics support the findings by Grant et al. (2010) that polarized 1.4 GHz sources tend to have structure at arcsecond scales and that, as a consequence, their polarized emission is unlikely to be beamed. Combined with our earlier classification from Fig. 3 of all polarized ATLAS sources as AGNs, and our interpretation from Fig. 6 that most or all polarized components are associated with AGN jets or lobes (rather than cores), the statistics above demonstrate

that (sub-)millijansky polarized sources tend to be extended jet- or lobe-dominated active radio galaxies. This conclusion is supported by the finding from Grant et al. (2010) that polarized sources tend to have steep spectra, which are characteristic of lobes.

In Fig. 8 we find that ATLAS DR2 sources typically have $LAS \lesssim 10''$, suggesting that most sources are located at $z \gtrsim 0.2$. This is consistent with the preliminary redshift distributions presented by Norris et al. (2006) and Middelberg et al. (2008) for ATLAS DR1 sources (see also discussion of radio source redshift distribution by Condon 1988).

Focusing on the panels in the lower-left corners of Fig. 7 and Fig. 8, we find that single- and multi-component sources are distributed approximately equally in fractional polarization space; their fractional polarization upper limits are not restrictive enough to identify any possible underlying trends. However, having found above that polarized sources are likely to represent lobed galaxies, it is perhaps surprising that we do not find a clear correlation between fractional polarization and LAS due to beam depolarization. Given the $\sim 10''$ resolution of ATLAS, in general a classical double radio source with dual polarized lobes should exhibit greater fractional polarization than a similar source with smaller LAS that is observed as a single-component source. A likely explanation may be that a significant number of the polarized single-component sources indicated in Fig. 7 are actually individual lobes of as-yet unassociated multi-component sources (see Section 6.1 of

¹ Note that surface brightness dimming, which is $\propto (1+z)^4$ (Tolman 1930; Sandage & Lubin 2001), may cause observed angular sizes of extended sources to be smaller than true sizes, due to faint source edges.

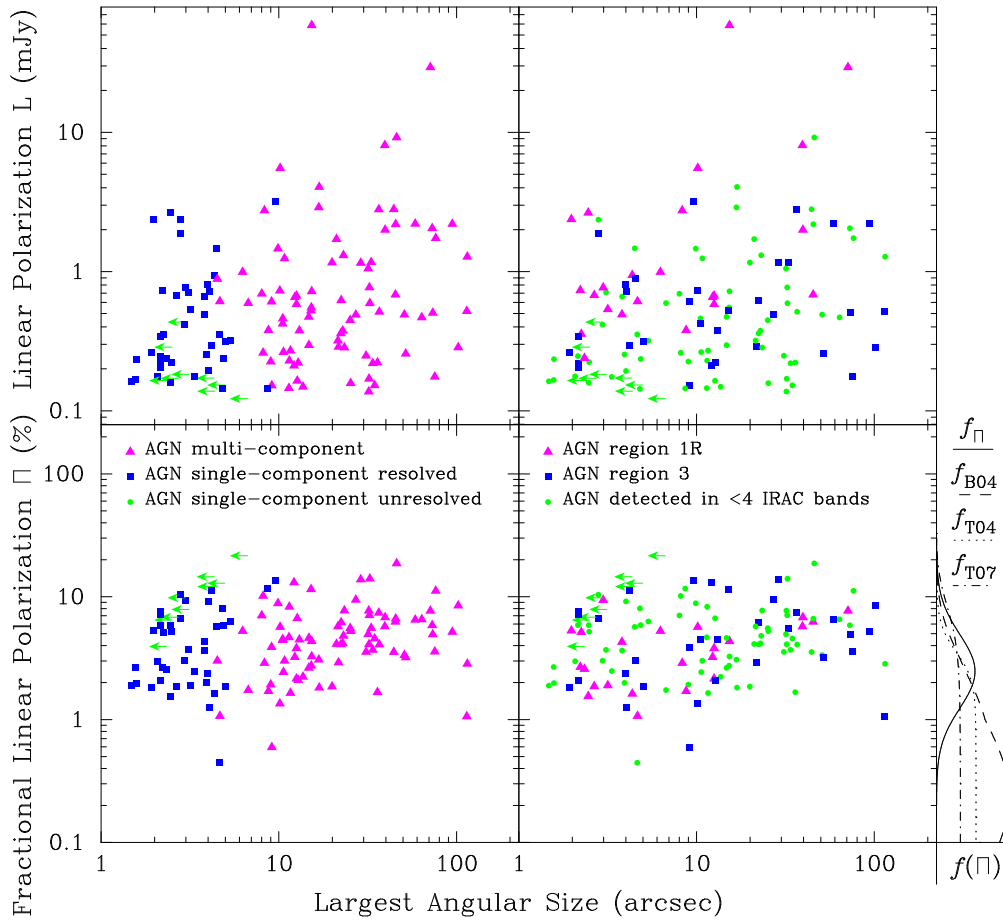


Figure 7. Linearly polarized flux density (upper panels) and corresponding fractional linear polarization (lower panels) versus LAS for all polarized ATLAS DR2 sources. For visual clarity, sources with polarization upper limits are not displayed here; they are presented separately in Fig. 8. Panels in the left column highlight sources according to their number of observed constituent components. Panels in the right column highlight sources according to the properties of their infrared counterparts where available, similar to those described for the data presented in the left column of Fig. 5. Note that all polarized ATLAS DR2 sources have been classified as AGNs. The curves adjacent to the lower-right panel replicate the fractional polarization distributions presented in Fig. 14 (see Section 2.4).

Paper I). Note that all single-component sources in Fig. 7 are classified as Type 4 in Fig. 9. Another potential explanation may be that for dual-lobed sources with small angular size observed as single-component sources, asymmetric depolarization between the lobes (Garrington et al. 1988; Laing 1988) could result in overall source fractional polarization levels similar to those of Type 7 sources (see Fig. 9), rather than resulting in significantly beam-depolarized (and thus perhaps unpolarized) sources overall.

The upper limits presented in the left column of Fig. 8 do not reveal any clear underlying trends within or between source classes. The multi-component sources classified as SFGs in Fig. 8, which are also shown located within the AGN parameter space in the lower-right panel of Fig. 3, require future study. These may represent composite sources exhibiting both AGN and SFG characteristics, for example similar to the ultra-luminous infrared galaxy F00183–7111 investigated by Norris et al. (2012) or the more general classes of post-starburst quasars (e.g. Cales et al. 2011).

Focusing on the right column of Fig. 7, we do not find any angular size distinctions between polarized sources based on their infrared colours. Furthermore, we find no underlying trends within the associated upper limit data from the right column of Fig. 8.

Focusing on Fig. 9, we find that Type 6 sources typically extend to greater angular sizes than Type 7 sources, though a larger

sample size with proportionally fewer Type 8 classifications is required to confirm this finding. We also find that each of the 3 polarized cores classified as Type 5 are resolved, and that they populate the same region of parameter space as Type 4 sources.

2.3 Differential Component Counts

We present Euclidean-normalised differential number-counts derived from the ATLAS DR2 total intensity and linear polarization component catalogues in Fig. 10 and Fig. 11, respectively, and in tabulated form in Appendix A. Counts for each bin have been plotted and tabulated at the expected average flux density, which we denote by S_{AV} , as given by Equation (19) from Windhorst, van Heerde, & Katgert (1984). This value takes into account the number-count slope and becomes important when assigning flux densities for bins containing few counts or with large widths in flux density space; S_{AV} only equals the bin geometric mean when $\gamma = 2$, where γ is the slope of the differential number counts $dN/dS \propto S^{-\gamma}$.

Bin widths for all total intensity counts were selected to be a factor of 0.07 dex for $I < 1$ mJy, 0.13 dex for $1 \leq I < 10$ mJy, and 0.2 dex otherwise. In linear polarization, bin widths were selected to be a factor of 0.16 dex for $L < 10$ mJy, and 0.3 dex otherwise.

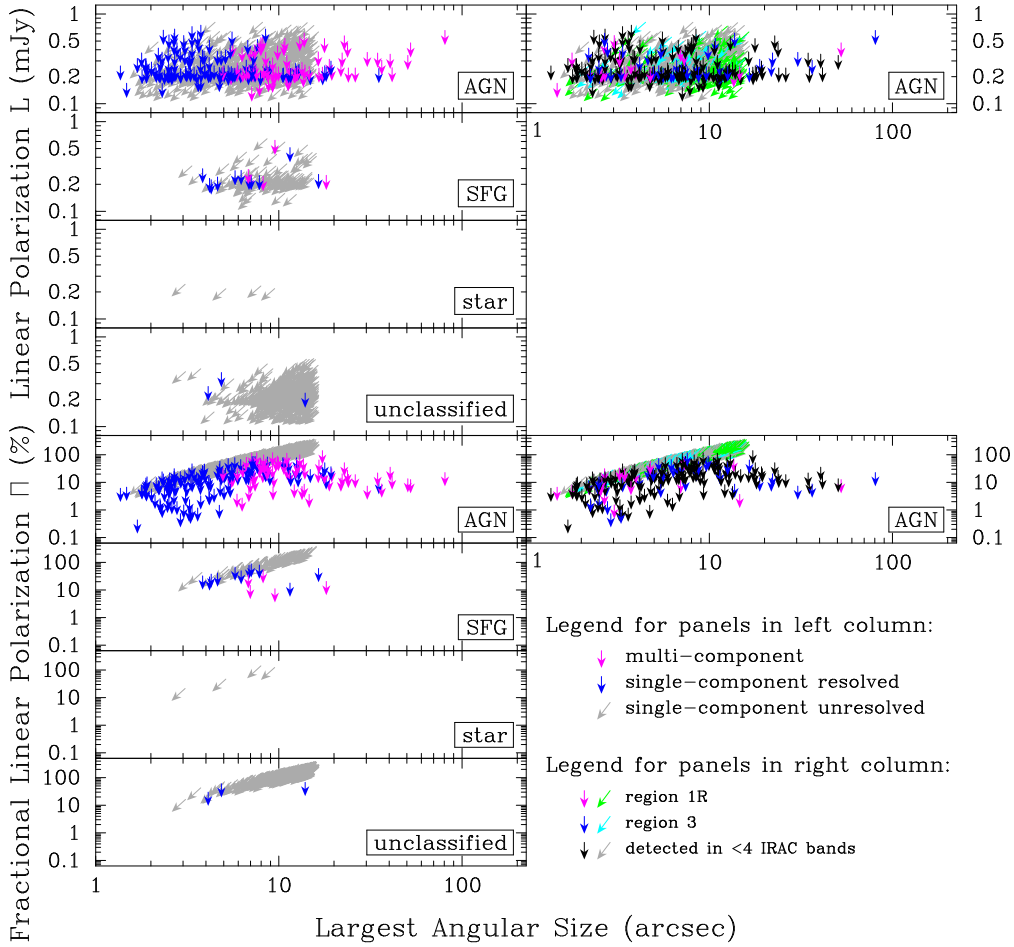


Figure 8. Polarization upper limits for sources omitted from Fig. 7. The 4 upper-left panels each correspond to the upper-left panel from Fig. 7 (though with different y-axis scaling), separated here into 4 source classes for clarity. Similarly, the upper-right panel corresponds to the upper-right panel from Fig. 7. Panels in the lower-half of the figure are similar to the upper-half panels, but for fractional polarization upper limits. Only sources classified as AGNs with infrared counterparts in regions 1R and 3 of Fig. 2, and those detected in less than 4 IRAC bands, are displayed in the right-column panels. In all panels, vertical arrows represent resolved sources, while diagonal arrows represent unresolved sources with deconvolved angular size upper limits.

We removed all bins containing components with visibility area corrections ≥ 10 , so as to prevent the number-counts from being dominated by the few components detected in the most sensitive and potentially least-representative regions of the ATLAS images. (Note that we did not remove individual offending components in order to retain the faintest bins, as this would have led to a bias in their resulting number-counts.) In total intensity this resulted in the removal of the faintest few bins containing ~ 30 components from each of the CDF-S component- and bin-corrected datasets, and ~ 20 components from each of the ELAIS-S1 component- and bin-corrected datasets. The maximum visibility area corrections for any components in the remaining valid CDF-S and ELAIS-S1 bins were 9.9 and 6.1, respectively. In linear polarization, the maximum visibility area corrections for any components in the CDF-S and ELAIS-S1 datasets were 7.9 and 3.7, respectively. As a result, we did not remove any bins in linear polarization.

Resolution and Eddington bias corrections were calculated in Section 7 of Paper I. The former was designed to correct for incompleteness to resolved components with low surface brightness, and for the redistribution of counts between bins resulting from systematic undervaluation of flux densities for components classified as unresolved. The latter was designed to correct for the redistribution of counts between bins due to random measurement errors

in the presence of a non-uniformly distributed component population. These bias corrections were calculated in Paper I by assuming that the true underlying differential number counts in total intensity were given by the sixth-order empirical fit to the Phoenix and FIRST surveys presented by Hopkins et al. (2003). This fit, which we denote H03, is given by

$$\log \left[\frac{dN_{\text{H03}}/dI}{I^{-2.5}} \right] = \sum_{j=0}^6 a_j \left[\log \left(\frac{I}{\text{mJy}} \right) \right]^j, \quad (3)$$

with $a_0 = 0.859$, $a_1 = 0.508$, $a_2 = 0.376$, $a_3 = -0.049$, $a_4 = -0.121$, $a_5 = 0.057$, and $a_6 = -0.008$. To illustrate the potential boosting effects of an exaggerated population of faint components, Paper I also defined a modified H03 distribution, denoted H03M, in which a Euclidean slope was inserted between $30\text{--}300\mu\text{Jy}$,

$$\frac{dN_{\text{H03M}}}{dI}(I) = \begin{cases} \frac{dN_{\text{H03}}}{dI}(I) & \text{if } I \geq 300 \mu\text{Jy} \\ \frac{dN_{\text{H03}}}{dI}(300 \mu\text{Jy}) & \text{if } 30 \leq I < 300 \mu\text{Jy} \\ \frac{dN_{\text{H03}}}{dI}(10 \times I) & \text{if } I < 30 \mu\text{Jy} \end{cases} \quad (4)$$

For bias corrections in linear polarization, we modelled the true underlying differential number counts dN/dL by convolving the total intensity H03 distribution from Equation (3) with a probability distribution for fractional linear polarization $f_{\Pi}(\Pi) \equiv f_{\Pi}(L/I)$,

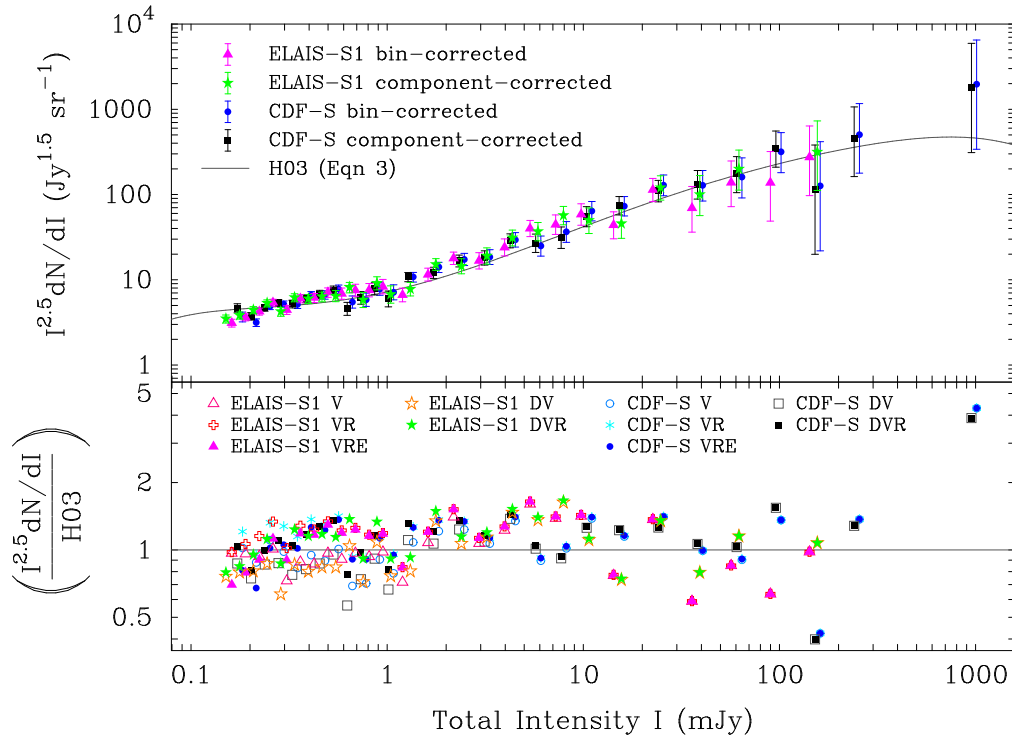


Figure 10. Euclidean-normalised differential component counts at 1.4 GHz in total intensity for the ATLAS CDF-S and ELAIS-S1 fields. *Upper Panel:* Fully corrected counts for each field resulting from the two alternative Eddington bias correction schemes applied in this work. Errors are 1σ Poissonian following Regener (1951). The solid curve represents the empirical fit from Hopkins et al. (2003), given by Equation (3). *Lower Panel:* Effects of resolution and Eddington bias corrections on differential component counts, relative to the H03 curve. For data associated with the bin-correction scheme for Eddington bias, counts are indicated following visibility area correction (V), resolution bias correction (VR), and finally all three corrections including the bin-value Eddington bias correction (VRE). For data associated with the component-correction scheme, counts are indicated following individual component deboosting and visibility area correction (DV), and finally the resolution bias correction (DVR). Note that the VRE and DVR points correspond to the points shown in the upper panel.

which we denote $H03 * f_{\Pi}$. The $f_{\Pi}(\Pi)$ distribution is presented in Equation (5) in Section 2.4.

The ATLAS DR2 component counts extend down to a flux density of approximately $140 \mu\text{Jy}$ in both total intensity and linear polarization. The brightest flux density bins are sparsely sampled because the ATLAS survey areas are not large enough to include significant numbers of increasingly rare bright components. In both Fig. 10 and Fig. 11 we find that the number-counts from the two separate ATLAS fields are consistent within the errors over their full observed flux density ranges. The impacts of the combined resolution and Eddington bias corrections on the number-counts appear to be relatively minor. In total intensity, the two corrections largely cancel each other out, while in linear polarization the resolution bias corrections dominate. In both total intensity and linear polarization, the combined corrections affect the underlying visibility area corrected counts by a factor of $\lesssim 0.5$, and do not affect the counts for $S \gtrsim 3 \text{ mJy}$. We find that differences between the two independent Eddington bias correction schemes are largely negligible for both the total intensity and linear polarization number-counts, providing confidence in these approaches.

In Fig. 10 we find that the total intensity counts closely follow the H03 model within a factor of $\sim 20\%$, though the ATLAS counts may begin to systematically drop below the H03 model for $S \lesssim 0.2 \text{ mJy}$. It is likely that the drop is caused by residual incompleteness in our resolution bias corrections, in turn caused by uncertainties regarding our assumed true angular size distribution for $\Theta < 3''$ as discussed in Section 7.1 of Paper I. However, we

note that if we assume that the Bondi et al. (2003) model presented in Fig. 19 of Paper I is the best representation of the true angular size distribution (without any flux density scaling), then the faintest bins at $S \approx 140 \mu\text{Jy}$ only require an additional correction factor of at most approximately $+30\%$. The faintest bins are therefore consistent with the H03 model.

As we do not find any systematic divergence between the ATLAS total intensity counts and the H03 model at the faintest flux densities (when accounting for the suspected residual resolution bias described above), we confirm that the H03 model is suitable for predicting 1.4 GHz component counts (and source counts as described below) down to at least $\sim 100 \mu\text{Jy}$ in surveys with resolution FWHM $\sim 10''$. Should we have found a systematic divergence, it would have indicated that our predicted Eddington bias corrections were unrealistic, and that in turn the H03 model underpinning these corrections formed an increasingly poor representation of the true number-counts for decreasing flux density. Under this hypothetical situation, an iterative approach would have been required in order to correctly identify an input true number-count model so as to bring about convergence with the fully corrected observed counts. In Section 7.2 of Paper I we predicted the levels of Eddington bias that would be present within the observed ATLAS counts if the true counts were given by the H03 or H03M models [the latter model contains a larger population of components with $S < 0.3 \text{ mJy}$ than the former; see Equation (4)]. We predicted that the H03M model would induce significantly greater Eddington bias at $S < 0.3 \text{ mJy}$ than the H03 model (see Fig. 23 in Paper I). There-

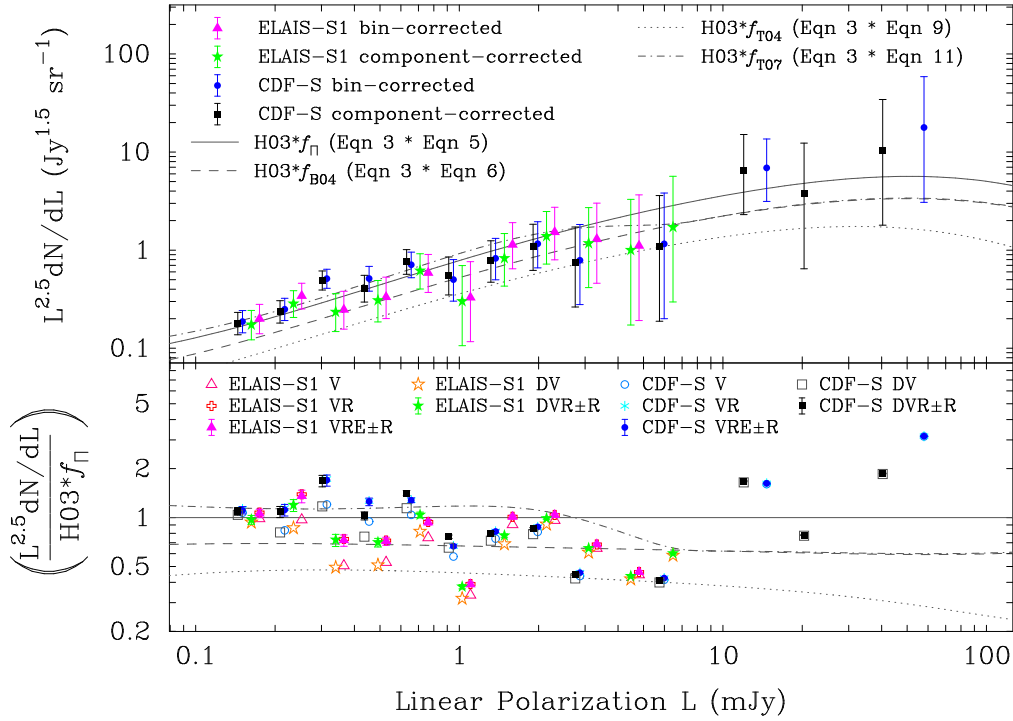


Figure 11. Euclidean-normalised differential component counts at 1.4 GHz in linear polarization for the ATLAS CDF-S and ELAIS-S1 fields. *Upper Panel:* Fully corrected counts for each field resulting from the two alternative Eddington bias correction schemes applied in this work. Errors are 1σ Poissonian following Regener (1951). The four curves indicate number-count predictions obtained by convolving the total intensity H03 curve with the various fractional polarization distributions presented in Fig. 14 (see Section 2.4). *Lower Panel:* Effects of resolution and Eddington bias corrections on differential component counts, relative to the $H03 * f_{\Pi}$ curve. The legend is similar to that presented in Fig. 10. Error bounds on the VRE and DVR points indicate uncertainties regarding the resolution bias correction factors (see Fig. 22 in Paper I).

fore, if the H03 model was used to predict the observed Eddington bias when in fact the H03M model best represented the true counts, then the observed counts would exhibit significant positive residual Eddington bias; if vice versa, the residual bias would be negative. Given that we do not observe a systematic rise (or fall) at faint flux densities in the fully corrected ATLAS counts (again accounting for the suspected residual resolution bias described above), we conclude that the H03M model is not supported by the ATLAS data. We note that the resolution bias corrections applied in this work are practically insensitive to changes between the H03 and H03M models. This is because for any given flux density bin, the resolution bias corrections are unaffected by the assumed form of the number-count distribution at fainter flux densities. Therefore, assuming that our resolution bias corrections are appropriate to begin with, we can focus on Eddington bias alone in order to draw the conclusions described above.

Below a flux density of ~ 1 mJy, we expect the ATLAS total intensity component counts to be dominated by single-component sources, with negligible contributions from components within multi-component sources. While we are unable to explicitly quantify this expectation given present data, we note that conservatively $< 30\%$ of all 2416 ATLAS components reside within multi-component sources (this fraction takes into account the number of components estimated to reside within as-yet unassociated multi-component sources; see Section 6.1 of Paper I). We expect that most of these multi-component sources represent FR II sources, which are known to dominate the source counts at flux densities $\gtrsim 10$ mJy and which diminish significantly below ~ 1 mJy (e.g. Wilman et al. 2008). At sub-mJy levels, radio sources in general are expected to have angular sizes $\sim 1''$; these are likely to be

observed as single-component sources in ATLAS. Therefore, we conclude that the ATLAS component counts may act as a suitable proxy for source counts at sub-mJy levels. We note that our characterisation of the faint component/source population using the H03 model in this work has relied on the similar resolutions of the ATLAS and Phoenix surveys. Should these resolutions have differed significantly, so too would have the properties of their observed components. Hopkins et al. (2003) obtained their model by using a sixth-order fit to the observed component counts from the Phoenix survey, supplemented at $S > 2.5$ mJy by source counts from the FIRST survey (White et al. 1997). The H03 model was thus intended to characterise source counts at all flux densities, despite being derived from a component catalogue at faint flux densities.

For $S > 2.5$ mJy, the ATLAS total intensity component counts follow the H03 model and thus the FIRST source counts. We explain this correspondence as follows by first presenting results that examine how source and component counts are expected to differ. Given that FR II sources dominate the source counts above ~ 10 mJy and that these sources are likely to comprise multiple components within a survey such as ATLAS, we expect the differential counts for sources to rise and extend to brighter flux densities than those for components. To roughly illustrate this behaviour and examine the difference between source and component counts in general, we considered an idealised scenario in which all sources were assumed to comprise two identical components, each with half the flux density of their parent. For illustrative purposes we assumed that the component count distribution was given by the H03 model. To derive the idealised differential source counts, we integrated the differential component counts to obtain integral component counts, divided these integral counts by two, doubled the flux

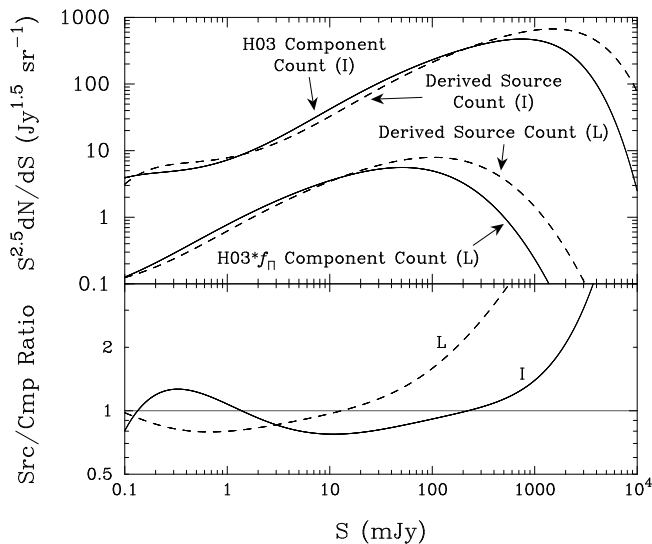


Figure 12. Idealised relationship between source counts and component counts in total intensity (I) and linear polarization (L). Dashed curves in the upper panel are derived from their respective solid curves by assuming that all I or L sources comprise two identical I or L components with half the flux density of their parents. Curves in the lower panel indicate the ratio between source and component counts for I and L. See Section 2.3 for details.

density scale, and differentiated. For completeness, we also derived differential source counts in linear polarization by following a similar procedure, where the relevant differential component counts were assumed to follow the $H03 * f_{\parallel}$ model. We present the resulting total intensity and linear polarization source counts in Fig. 12. We find that the predicted source counts remain within $\sim 30\%$ of the component counts across the flux density ranges probed by the ATLAS data in total intensity ($I \lesssim 1$ Jy) and linear polarization ($L \lesssim 100$ mJy). (Separately, while not shown, we note that the integral counts for both components and sources within our rudimentary model are very similar, for both total intensity and linear polarization.) As expected, at bright flux densities the component counts drop below the source counts, though these drops occur at brighter flux densities than relevant to the ATLAS data. Note that in reality, the differential source and component counts are likely to overlap more closely than presented in Fig. 12 because of the presence of single-component sources. Thus we conclude that for surveys with resolution FWHM $\sim 10''$ similar to Phoenix and ATLAS, the H03 model may be used to characterize both component and source counts in total intensity for $S \lesssim 1$ Jy.

We conjecture that, as modelled above, the H03 model characterises component rather than source counts at all flux densities, including at $S > 1$ Jy. To justify this claim, we note that components in the FIRST survey were only grouped into multi-component sources if they were located within $50''$ (White et al. 1997). From Fig. 7 of this work we can see that a cutoff of $50''$ is likely to be too small to capture sources with the most widely-separated components, which are also likely to be the brightest sources. In addition, flux densities for extended FIRST components are likely to be underestimated due to insensitivity to extended emission. Therefore, the FIRST source counts are likely to be deficient at the brightest flux densities. Incidentally, the FIRST source counts and thus the H03 model appear to form a suitable hybrid distribution for describing component counts at all flux densities in surveys with resolution FWHM $\sim 10''$ such as ATLAS. We may therefore conclude that the $H03 * f_{\parallel}$ model is suitable for characterising com-

ponent counts in linear polarization at all flux densities, not just at $L \lesssim 100$ mJy where differences between polarized component and source counts are likely to diminish as shown in Fig. 12. If the H03 model were to better represent source counts rather than component counts at $I > 1$ Jy, then the polarized counts resulting from convolution with f_{\parallel} would reside ambiguously between a component and source count distribution for $L \gtrsim 5$ mJy. Thus it would be inappropriate to estimate integral component or source counts from the $H03 * f_{\parallel}$ (or indeed H03) model; this point is relevant to results presented shortly.

In Fig. 11 we find that the ATLAS linear polarization component counts steadily decline with decreasing flux density, as generally predicted by all four models displayed in the background. The solid curve displays our assumed true component count model, namely $H03 * f_{\parallel}$, which we used to derive the corrections for resolution and Eddington bias. The fully corrected ATLAS counts closely follow this model within statistical error, indicating consistency between the model, the corrections, and the observational data. Each of the four background models in Fig. 11 were calculated by convolving the H03 model with a fractional polarization distribution. We note that these convolutions are only appropriate because, as described above, the H03 model appears to appropriately characterise the total intensity component counts at all flux densities relevant to ATLAS. In Section 2.4 we describe each of the fractional polarization distributions underlying the four background models, and compare their abilities to predict the ATLAS polarized counts and polarization data in general.

The number of polarized components expected per square degree at or brighter than a given flux density, as constrained by the observed ATLAS component counts, can be estimated by integrating the $H03 * f_{\parallel}$ polarized count distribution (the solid curve in Fig. 11). The resulting integral component counts are displayed in Fig. 13. We estimate that the sky density of polarized components for $L \geq 200 \mu\text{Jy}$ is 30 deg^{-2} , for $L \geq 100 \mu\text{Jy}$ it is 50 deg^{-2} , and for $L \geq 50 \mu\text{Jy}$ it is 90 deg^{-2} . If we make the rudimentary assumption described earlier regarding Fig. 12 that every polarized component belongs to a dual-component source with double the flux density, we can estimate the integral source count distribution; this is displayed alongside the integral component count distribution in Fig. 13. We thus estimate that the sky density of polarized sources for $L \geq 200 \mu\text{Jy}$ is $\sim 25 \text{ deg}^{-2}$, and for $L \geq 100 \mu\text{Jy}$ it is $\sim 45 \text{ deg}^{-2}$. We expect that these integral source count estimates are accurate to within 10%, even if a more suitable model incorporating polarized single-component sources is utilised.

2.4 Distribution of Fractional Linear Polarization

In this section we present a model to describe the distribution of fractional polarization for AGN sources and their components/groups observed at 1.4 GHz in surveys with resolution FWHM $\gtrsim 10''$, as constrained by the ATLAS DR2 data.

There appears to be a significant overlap between the fractional polarization properties of all classification Types representing both components/groups and sources in Fig. 6. Taking into account the presence of upper limits (see Fig. 4), we find that typical levels of fractional polarization are concentrated between 0.4% and 20%, regardless of whether the focus is on sources or on their constituent components/groups. Given this apparent overlap, we assume for simplicity that the distribution of fractional polarization for both components/groups and sources can be modelled using the same PDF, which we denote by $f_{\parallel}(\Pi)$. Before presenting our model for this distribution, we note three caveats. First, fol-

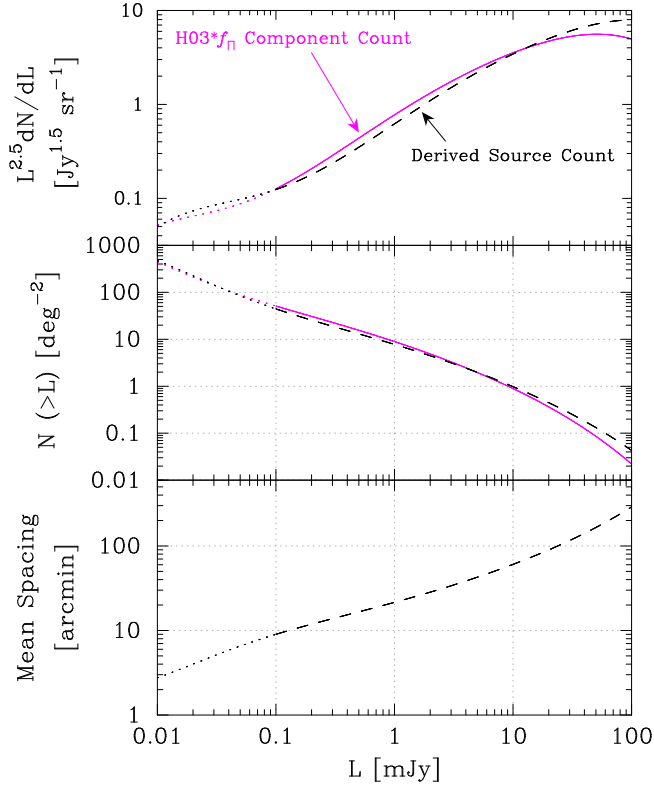


Figure 13. *Upper panel:* Reproduction of linearly polarized component and source counts from Fig. 12. The dotted portions of the curves at $L < 0.1$ mJy indicate extrapolations beyond the observed ATLAS DR2 data, assuming an unchanging distribution of fractional polarization (though note comments in Section 2.4). *Middle panel:* Estimated sky density for components and sources above a given linearly polarized flux density. *Lower panel:* Mean spacing between linearly polarized sources as a function of the faintest detected sources.

lowing our conclusions presented in Section 2.2 regarding potential correlation of the distribution of fractional polarization with total flux density, we assume that $f_{\Pi}(\Pi)$ is independent of total intensity flux density. This assumption may not be suitable for $I \lesssim 10$ mJy for which our ATLAS data become sparse. Second, our model for $f_{\Pi}(\Pi)$ may only be relevant for surveys with resolution FWHM $\gtrsim 10''$. Surveys with finer resolution may encounter less beam depolarization across components, and thus recover higher average levels of fractional polarization (in Section 5 of Paper I we found that $< 17\%$ of polarized ATLAS components were resolved). We note that surveys with coarser resolution will incur increased blending between components within multi-component sources, resulting in a greater number of low- Π sources than observed for ATLAS due to enhanced beam depolarization. And third, given that all polarized components in ATLAS DR2 are associated with AGNs, we restrict our model for $f_{\Pi}(\Pi)$ to the characterisation of AGNs, rather than the characterisation of all radio sources including SFGs and individual stars. We do not attempt to differentiate between different types of AGNs or their components within our model, i.e. FRI/FRII/radio quiet/core/lobe. We discuss fractional polarization levels for SFGs in Section 3.2.

We modelled $f_{\Pi}(\Pi)$ by qualitatively fitting two independent sets of ATLAS data: (i) the fractional polarizations of components, groups, and sources displayed in Fig. 4, importantly taking into account upper limits, and (ii) the differential number-counts for polarized components displayed in Fig. 11. We obtained a concordance

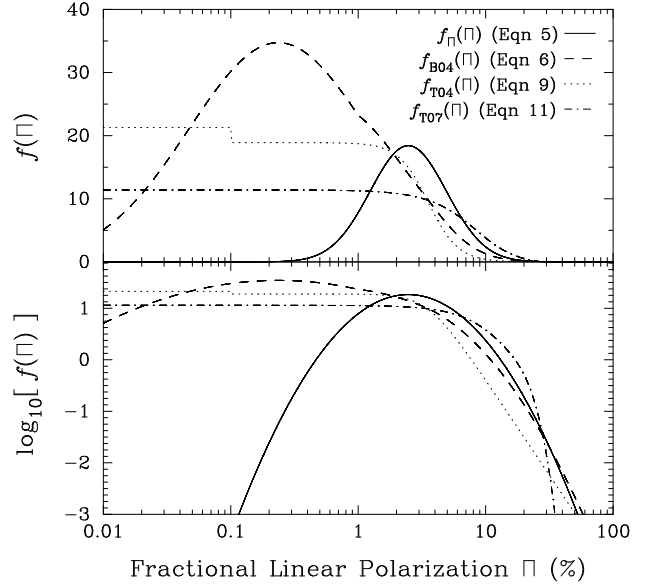


Figure 14. Proposed models of 1.4 GHz fractional linear polarization; see Section 2.4 for details. The solid curve represents a fit to the ATLAS DR2 data, and is the distribution assumed in this work. The vertical axis is linear in the upper panel and logarithmic in the lower panel. The curves presented here are compared to the fractional polarization data in Fig. 4 (also Fig.'s 5-7 and 9) and to the number count data in Fig. 11 (also Fig. 16).

fit to these data by modelling $f_{\Pi}(\Pi)$ using a log-normal distribution,

$$f_{\Pi}(\Pi) = \frac{1}{\Pi \sigma_{10} \ln(10) \sqrt{2\pi}} \exp \left\{ -\frac{[\log_{10}(\Pi/\Pi_0)]^2}{2\sigma_{10}^2} \right\}, \quad (5)$$

where the parameters Π_0 and σ_{10} are the median fractional polarization and scale parameter, respectively, given by best-fit values $\Pi_0 = 4.0\%$ and $\sigma_{10} = 0.3$. The fit given by Equation (5) is consistent with the result obtained by analysing the fractional polarization data alone, using the product-limit estimator (Kaplan & Meier 1958) as implemented within the `survival`² package in the R³ environment. The mean level of fractional polarization for the distribution in Equation (5) is given by $\log_{10} \mu_{\Pi} = \log_{10}(\Pi_0) + 0.5 \ln(10) \sigma_{10}^2$, which equates to $\mu_{\Pi} = 5.1\%$. For values of Π_0 or σ_{10} larger than the best-fit values above, we found that the H03 * f_{Π} model predicted differential counts in excess of the observed ATLAS counts. For smaller values, the predicted counts were deficient.

We plot Equation (5) in Fig. 14. For comparison we also plot the 1.4 GHz fractional polarization distributions proposed by Beck & Gaensler (2004), Tucci et al. (2004), and Taylor et al. (2007). For clarity we explicitly document each of these distributions, as follows. Beck & Gaensler (2004) investigated the distribution of fractional polarization for NVSS sources with $I > 80$ mJy, which they fit using the following quasi log-normal form,

$$f_{B04}(\Pi) = \frac{a_{B04}}{\Pi \ln(10)} \exp \left\{ -\frac{[\log_{10}(\Pi/\Pi_{B04})]^2}{2\sigma_{B04}^2} \right\}, \quad (6)$$

² <http://cran.r-project.org/web/packages/survival/index.html>

³ <http://www.r-project.org>

where

$$a_{B04} = \begin{cases} 0.690 & \text{if } \log_{10} \Pi \leq -2 \\ 0.808 & \text{if } \log_{10} \Pi > -2, \end{cases} \quad (7)$$

$$\sigma_{B04} = \begin{cases} 0.700 & \text{if } \log_{10} \Pi \leq -2 \\ 0.550 & \text{if } -2 < \log_{10} \Pi \leq -1.5 \\ 0.353 & \text{if } \log_{10} \Pi > -1.5, \end{cases} \quad (8)$$

and where $\log_{10} \Pi_{B04} = -1.5$. The median and mean fractional polarization levels of the f_{B04} distribution are 2.1% and 3.3%, respectively. Similarly, Tucci et al. (2004) investigated the distribution of fractional polarization for NVSS sources with $I > 100$ mJy, which they fit using the following monotonic form,

$$f_{T04}(\Pi) = 1.32 \left\{ a_{T04} [2.7 + 0.025 (100 \Pi)^{3.7}]^{-1} + b_{T04} \right\} \quad (9)$$

where $a_{T04} = 51$,

$$b_{T04} = \begin{cases} 2.4 & \text{if } \Pi \leq 0.1 \\ 0 & \text{if } \Pi > 0.1, \end{cases} \quad (10)$$

and where we have included a correction factor of 1.32 to ensure that the distribution is normalised. The median and mean fractional polarization levels of the f_{T04} distribution are 2.1% and 2.7%, respectively. Taylor et al. (2007) fit the distribution of fractional polarization for sources with $I < 30$ mJy in the ELAIS-N1 field by modifying a Gram-Charlier series of type A (e.g. van der Marel & Franx 1993), resulting in the following monotonic form,

$$f_{T07}(\Pi) = \begin{cases} 11.06 \exp\left(\frac{-\Pi^2}{2\sigma_{T07}^2}\right) \left\{ 1 + \frac{h_4}{\sqrt{24}} \left[4\left(\frac{\Pi}{\sigma_{T07}}\right)^4 - 12\left(\frac{\Pi}{\sigma_{T07}}\right)^2 + 3 \right] \right\} & \text{if } I < 30 \text{ mJy} \\ f_{B04}(\Pi) & \text{if } I \geq 30 \text{ mJy}, \end{cases} \quad (11)$$

where $\sigma_{T07} = 0.07$, $h_4 = 0.05$, and where we have included a correction factor of 11.06 to ensure that the distribution is normalised. For $I \geq 30$ mJy, Taylor et al. (2007) found that the ELAIS-N1 data were consistent with the f_{B04} distribution from Equation (6). The median and mean fractional polarization levels of the f_{T07} distribution for $I < 30$ mJy are 4.8% and 6.0%, respectively.

The four curves presented in Fig. 14 are replicated in Figs. 4–7 and Fig. 9. The four curves are also presented in Figs. 11 and 16 following convolution with the H03 differential count model. In Fig. 16 we find that the fractional polarization distributions proposed by Beck & Gaensler (2004), Tucci et al. (2004), and Taylor et al. (2007) are in general agreement with the observed ATLAS polarized number counts. The models predict polarized counts that are within a factor of 5 of each other, and they all pass within a few standard errors of the ATLAS data points. However, we find that these three distributions are incompatible with the observed distribution of fractional polarization for ATLAS components, groups, sources, and in particular upper limits as presented in Fig. 4. The extended tails below $\Pi < 1\%$ for the distributions proposed by Beck & Gaensler (2004) and Tucci et al. (2004) are likely to reflect the various systematic biases we described earlier in Section 2.2 regarding the NVSS data. Polarized flux densities for NVSS sources were recorded regardless of whether or not the measurements met statistical criteria for formal detection. If upper limits were calculated for the NVSS data following a similar procedure to that described for the ATLAS data in Section 6.2 of Paper I,

then we suspect that far fewer detections strictly implying $\Pi < 1\%$ would have been made. We note that the f_{Π} model proposed in this work peaks at $\Pi \approx 2.5\%$, which is consistent with the NVSS data for $\Pi > 1\%$ from Mesa et al. (2002) and Tucci et al. (2004). The extended tail below $\Pi < 1\%$ in the Taylor et al. (2007) model reflects their assumption that the distribution peaks at $\Pi = 0$ and declines monotonically with increasing Π . The ATLAS DR2 data do not support this assumption.

As noted earlier, a caveat of the f_{Π} model is that it may not be suitable for $I \lesssim 10$ mJy, because the upper limits presented in Fig. 4 do not constrain the behaviour of the true fractional polarization distribution for low values of Π . However, given that the maximum level of fractional polarization exhibited by ATLAS components and sources appears to be limited to $\Pi \lesssim 20\%$, and given that this limit appears to be uncorrelated with flux density down to at least ~ 1 mJy (see comments regarding Fig. 5 in Section 2.2), we may draw tentative conclusions regarding the true distribution of fractional polarization for $1 \lesssim I \lesssim 10$ mJy. The ATLAS DR2 data are consistent with 3 general alternatives. First, the f_{Π} distribution may remain unchanged for $I < 10$ mJy. Second, for decreasing I , the mean of f_{Π} may decrease while its dispersion increases so as to maintain an approximately constant level of fractional polarization for outliers with large Π . And third, for decreasing I , the mean of f_{Π} may increase while its dispersion decreases. More sensitive observations are required to distinguish between these alternatives.

3 DISCUSSION

3.1 Comparison of Component Counts to Other Deep Surveys

In Fig. 12 of Section 2.3 we demonstrated that differences between differential number-counts of components and sources within a survey such as ATLAS are likely to be negligible below ~ 1 Jy in total intensity, and below ~ 100 mJy in linear polarization. We may therefore directly compare the ATLAS DR2 component counts with source counts from the literature in both total intensity and linear polarization. We present these comparisons in the following two sections.

3.1.1 Total Intensity

In Fig. 15 we compare the ATLAS DR2 bin-corrected total intensity component counts (from Fig. 10 or tabulated data from Appendix A) with source counts from other 1.4 GHz surveys of comparable sensitivity. These include the B1301+3034 field (Mitchell & Condon 1985), the HDF-N, Lockman Hole, and ELAIS-N2 fields (Biggs & Ivison 2006), the SSA13 field (Fomalont et al. 2006), the J1046+5901 field (Owen & Morrison 2008, hereafter OM08), a revised survey of the Lockman Hole (Ibar et al. 2009), the GOODS-N field (Morrison et al. 2010), the CDF-S field observed with the VLA (Padovani et al. 2011), and the ATLAS fields with counts at $S > 8$ mJy (Subrahmanyam et al. 2010) and deeper counts (Thorat et al. 2013).

At high flux densities the source counts are dominated by luminous radio galaxies and quasars. The flattening of the source counts below 1 mJy is produced by the emerging dominance of a population of sources comprised of radio-quiet AGNs (AGNs lacking significant jets and dominated in the radio band by non-thermal emission), low-power radio-loud AGNs, and star forming galaxies (Jarvis & Rawlings 2004; Simpson et al. 2006; Smolčić et al.

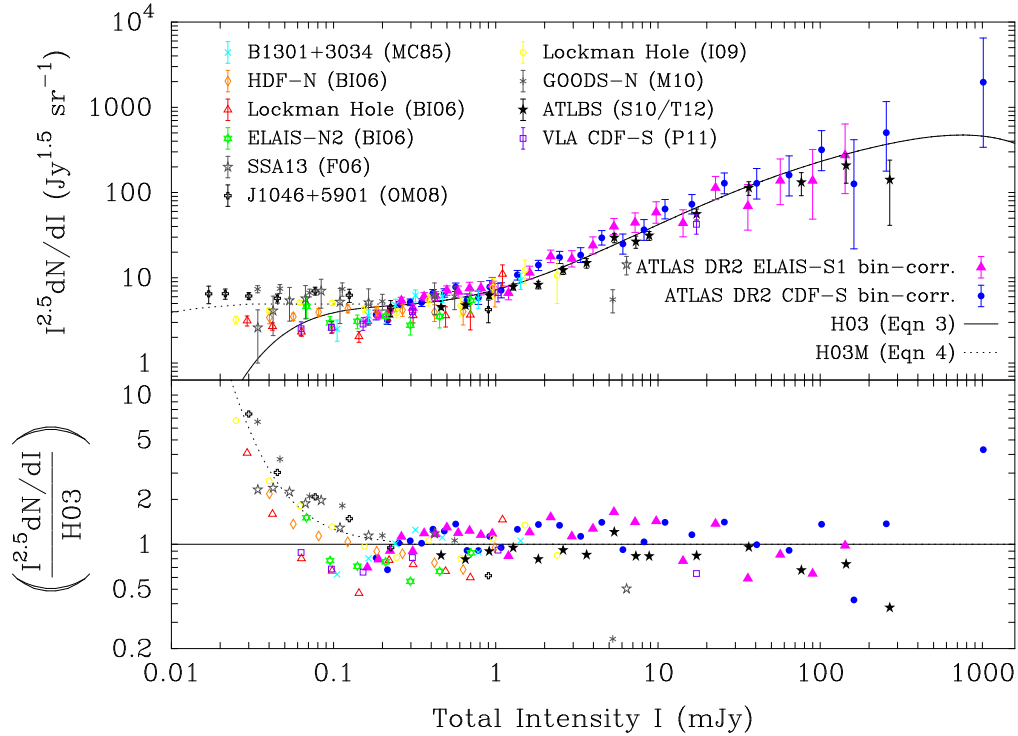


Figure 15. Comparison of ATLAS DR2 bin-corrected total intensity component counts with 1.4 GHz source counts from other surveys; see Section 3.1.1 for reference details. The panel layout follows Fig. 10. The solid and dotted curves represent the H03 and H03M models given by Equations (3) and (4), respectively. Data from the upper panel are reproduced in the lower panel relative to the H03 curve.

2008; Gendre & Wall 2008; Padovani et al. 2011). The extent to which the source counts flatten is somewhat controversial because counts from deep surveys appear to exhibit a large degree of scatter, for example as seen in Fig. 15 where there is a factor of 2 variation in the counts below 1 mJy. Measurements at 3 GHz from the Absolute Radiometer for Cosmology, Astrophysics, and Diffuse Emission (ARCADE) 2 balloon-borne experiment have indicated a temperature for the radio background about five times that previously expected from known populations of radio sources (Fixsen et al. 2011; Seiffert et al. 2011), which if not due to a residual calibration error (Subrahmanyan & Cowsik 2013) suggest the presence of a new population of faint ($< 10 \mu\text{Jy}$ at 1.4 GHz) or diffuse (few Mpc in extent) extragalactic sources (Singal et al. 2010; Vernstrom, Scott, & Wall 2011; Condon et al. 2012; Holder 2014).

Some studies have attributed the large scatter in the faint counts to cosmic variance, namely to intrinsic differences between survey fields caused by large scale structure (e.g. Seymour, McHardy, & Gunn 2004). However, significant differences in the counts for fields observed in separate studies, such as the GOODS-N field (located within the HDF-N field) or the Lockman Hole (see Fig. 15), indicate that data processing and calibration errors may be entirely responsible for the scatter (e.g. Ibar et al. 2009). By considering the consistent power-law form of the angular correlation function for both NVSS and FIRST sources obtained by Blake & Wall (2002) and Overzier et al. (2003), Massardi et al. (2010) estimated the cosmic variance for millijansky radio sources to be $\sigma_v^2 = 2.36 \times 10^{-3} \Omega^{-0.4}$ where Ω is the survey area in square degrees. The total variance for each source count bin containing N sources is then given by $N(1 + N\sigma_v^2)$, which includes Poisson chance. For a survey with $\Omega > 0.5 \text{ deg}^2$ and $N < 100$, cosmic variance contributes $< 15\%$ to the total rms uncertainty for each bin (this is consistent with a similar esti-

mate presented by Simpson et al. 2006 and a more detailed analysis by Heywood, Jarvis, & Condon 2013). The clustering behaviour of sub-millijansky sources is likely to be similar to that of millijansky sources (Overzier et al. 2003; Fine et al. 2011), or perhaps even less clustered (Negrello, Magliocchetti, & De Zotti 2006), in which case the cosmic variance contribution estimated above represents a conservative upper limit. The error bars for many of the faintest counts in Fig. 15 require enlargement by factors much larger than $\sim 15\%$ to become consistent with each other within a few standard errors. Our experience in constructing source counts for ATLAS suggests to us that there are a large number of data processing procedures that, if not carefully implemented, could easily give rise to significant systematic biases of order the observed scatter in the faint counts. We therefore agree with previous conclusions in the literature (e.g. Biggs & Ivison 2006; Simpson et al. 2006; Condon 2007; Ibar et al. 2009; de Zotti et al. 2010; Condon et al. 2012; Heywood, Jarvis, & Condon 2013) that the observed scatter in the sub-millijansky counts is likely to be significantly affected by data processing differences between surveys.

The ATLAS data support the H03 model down to $\sim 100 \mu\text{Jy}$ and rule out any flattening above this level; flattening similar to the H03M model is ruled out by a lack of residual Eddington bias. However, the DR2 data are not sensitive enough to support or refute the general trend of flattening reported by deeper surveys. Recently, Condon et al. (2012) used the probability of deflection technique [$p(D)$; Scheuer 1957] and a spectral index conversion to investigate the behaviour of the 1.4 GHz source counts at $2 - 20 \mu\text{Jy}$ within a confusion-limited observation of the OM08 J1046+5901 field at 3 GHz. By combining the results from a similar $p(D)$ analysis performed by MC85, Condon et al. (2012) ruled out any flattening or an upturn in the 1.4 GHz Euclidean counts between $2 \mu\text{Jy}$ and $100 \mu\text{Jy}$, such as that reported by OM08 or proposed to account

for the ARCADE 2 results (Seiffert et al. 2011; Singal et al. 2010; Vernstrom, Scott, & Wall 2011).

3.1.2 Linear Polarization

In Fig. 16 we compare the ATLAS DR2 bin-corrected linear polarization component counts (from Fig. 11 or tabulated data from Appendix A) with the 1.4 GHz polarized source counts from the NVSS (Tucci et al. 2004) and the ELAIS-N1 field (Taylor et al. 2007; deeper counts from Grant et al. 2010). The ATLAS DR2 counts improve upon the Grant et al. (2010) study by a factor of ~ 2 in sensitivity. The observed number-counts from the Tucci et al. (2004), Taylor et al. (2007), and Grant et al. (2010) studies are in general agreement with the ATLAS counts, though the ATLAS data do not exhibit flattening at faint levels that might otherwise lead to suggestions of increasing levels of fractional polarization with decreasing flux density or perhaps the emergence of a new source population. The flattening of the data from these studies are unlikely to be real, but rather probably reflective of spurious populations of sources with abnormally high levels of fractional polarization as described earlier in Section 2.2. This explains the difficulty encountered by O’Sullivan et al. (2008) in attempting to model the flattening. Similarly, despite the apparent consistency between the observed counts and the various predicted curves displayed in Fig. 16, in Section 2.4 we found that the fractional polarization distributions presented by Tucci et al. (2004), Taylor et al. (2007), and Grant et al. (2010) were inconsistent with the ATLAS data and therefore unlikely to be suitable for population modelling.

The flux density range over which the $H03 * f_{\Pi}$ model extends in Fig. 16 corresponds to the brightest regions of the total intensity counts, in which luminous radio galaxies and quasars dominate. This is consistent with our independent conclusion from Section 2.2 that the polarized sources contributing to the ATLAS counts tend to be FRI/II radio galaxies, and with our earlier findings regarding the infrared colours of polarized sources from Section 2.1.2. To fully confirm this picture, luminosity functions for polarized sources of different classifications need to be constructed (e.g. FRI/FRII/radio-quiet), which can then be compared with theory (e.g. O’Sullivan et al. 2008).

Very recently, while we were finalising this manuscript for resubmission, Rudnick & Owen (2014) published a similar study of faint polarized sources. Rudnick & Owen (2014) presented 1.4 GHz linearly polarized integral (not differential) source counts from the GOODS-N field, observed with the VLA at $1.6''$ resolution. Their polarized counts extend to $20 \mu\text{Jy}$, an order of magnitude deeper than our ATLAS DR2 results. Qualitatively, their results are consistent with our main finding that the fractional polarization levels of faint sources are not anti-correlated with total flux density. Quantitatively, however, their results are discrepant with ours. Rudnick & Owen (2014) predict that surveys with $10''$ resolution will observe a polarized source density of 22 deg^{-2} for $L \geq 100 \mu\text{Jy}$; this is a factor of 2 lower than the directly observed counts presented in this work. Rudnick & Owen (2014) explain that it is difficult to directly compare polarized source counts from surveys with $1.6''$ and $10''$ resolutions, but they consider a factor of 2 difference to be optimistically large (this factor was used to form their $10''$ resolution prediction). Given that Rudnick & Owen (2014) use peak surface brightness measurements as a proxy for flux density irrespective of source angular size, that they do not attempt to correct their data for effects such as resolution bias, and that they do not present total intensity counts with similar processing as for their linear polarization counts, it is difficult to assess

the robustness of their results here. Detailed assessment is beyond the scope of this work, and is better suited to future studies when results from other deep polarization surveys or modelling efforts become available.

3.2 Star-Forming Galaxies

We did not detect any polarized SFGs in this work. The fractional polarization upper limits for individual SFGs presented in the lower-right panel of Fig. 5 indicate that characteristic Π levels for the sub-millijansky ($I \gtrsim 100 \mu\text{Jy}$) SFG population are likely to be typically less than $\sim 60\%$.

Given that SFGs are only expected to begin contributing significantly to the total intensity source counts at $I \lesssim 100 \mu\text{Jy}$ (e.g. see Fig. 5; see also Wilman et al. 2008; Padovani et al. 2011), the limit above indicates that the $H03 * f_{\Pi}$ model is unlikely to be affected by the presence of SFGs unless $L \lesssim 60 \mu\text{Jy}$. Our limit of $\Pi_{\text{SFG}} < 60\%$ is consistent with the fractional polarization distribution for 1.4 GHz SFGs predicted by Stil et al. (2009); see panel (b) of Fig. 6 from their work. Stil et al. (2009) modelled the integrated polarized emission of spiral galaxies, finding typical fractional polarization levels of $< 5\%$ with overall mean level $< 1\%$. The $H03 * f_{\Pi}$ number-counts predicted in this work are therefore likely to represent an upper limit to the true polarized number-counts at μJy levels, due to the diminished mean level of fractional polarization for faint radio sources with respect to the f_{Π} model. More sensitive observations are required to detect polarized emission from faint SFGs and to quantify their polarization properties.

3.3 Asymmetric Depolarization in Double Radio Sources

Garrington et al. (1988) and Laing (1988) discovered that double radio sources depolarize less rapidly with increasing wavelength on the side with the brighter (or only) radio jet than on the opposite side, providing strong evidence that the apparent one-sided nature of jets in otherwise symmetric radio galaxies and quasars is caused by relativistic beaming. This ‘Laing-Garrington’ effect is typically interpreted as being caused by orientation-induced path-length differences through a foreground, turbulent, magnetised intragroup or intracluster medium which surrounds the entire radio source, where the approaching side is seen through less of this medium (Garrington & Conway 1991; Tribble 1991, 1992; Ensslin et al. 2003; Laing et al. 2008; Kuchar & Enßlin 2011). However, this interpretation is not unambiguous. The asymmetric depolarization effect may be contaminated or even dominated by depolarization internal to the lobes (O’Sullivan et al. 2013; Stawarz et al. 2013), a sheath mixing layer at the interface where relativistic and thermal plasmas meet (Bicknell, Cameron, & Gingold 1990; Johnson, Leahy, & Garrington 1995; Rudnick & Blundell 2004; Feain et al. 2009), draping of undisturbed intracluster magnetic fields over the surface of a lobe expanding subsonically (Dursi & Pfrommer 2008) or supersonically (Guidetti et al. 2011; Huarte-Espinosa, Krause, & Alexander 2011; Guidetti et al. 2012), or by intrinsic asymmetries in local environment which act separately or in addition to orientation-induced depolarization (Liu & Pooley 1991a,b; McCarthy, van Breugel, & Kapahi 1991; Ishwara-Chandra et al. 1998; Gopal-Krishna & Wiita 2004; Kharb et al. 2008).

In reality, it is likely that each of the mechanisms above may contribute, requiring a ‘unification scheme’ to predict which will dominate for any given source. For example, Guidetti et al. (2012)

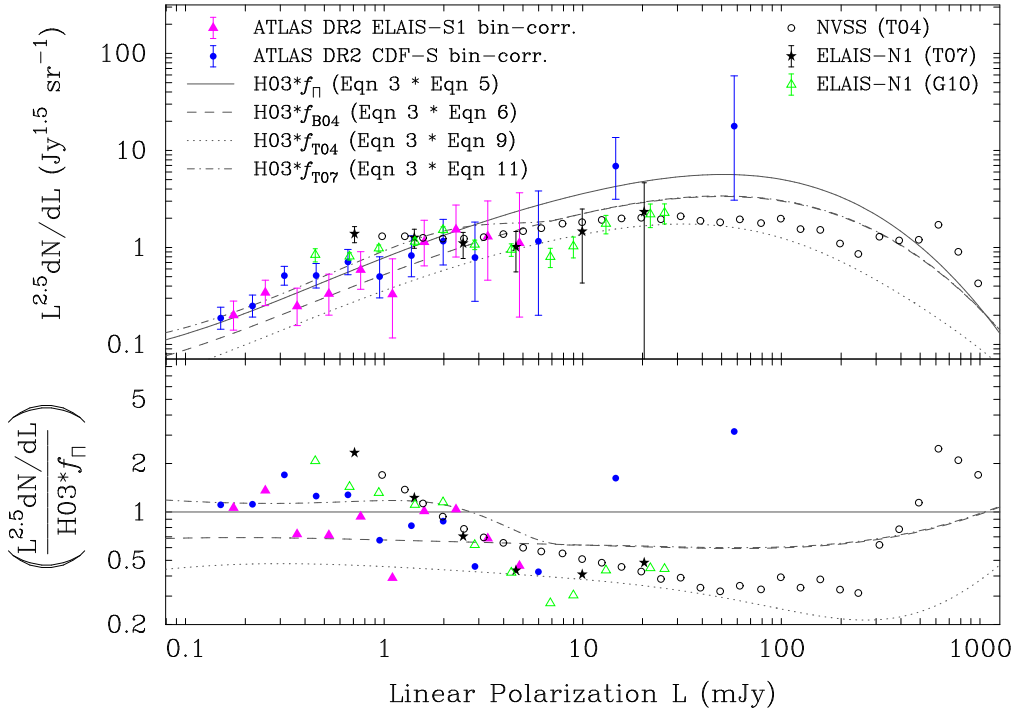


Figure 16. Comparison of ATLAS DR2 bin-corrected linear polarization component counts with 1.4 GHz source counts from other surveys; see Section 3.1.2 for details. The four number-count curves and panel layout follow Fig. 11. Data from the upper panel are reproduced in the lower panel relative to the $H03 * f_{\Pi}$ curve.

describes an emerging picture that differentiates between properties expected for FRI and FRII sources, and that includes an inner depolarization region associated with shells of dense thermal plasma around the radio jets in addition to the undisturbed intergalactic medium surrounding the source. However, this picture does not yet include variations on the general orientation-induced depolarization effect due to source environment asymmetries, such as the correlation between lobe properties and optical line emission described by McCarthy, van Breugel, & Kapahi (1991).

If the Laing-Garrington effect is caused predominantly by source orientation, rather than asymmetries in source environment, then we expect the fractional surface density of sources exhibiting asymmetric depolarization in a volume-limited sample to approximately relate to the fraction of randomly-oriented sources with $S \gtrsim 10$ mJy that are pointed towards Earth. We justify this expected relationship by noting that FRII sources are dominated by un-beamed lobe emission rather than jet emission which may be beamed, FRII sources dominate FRI sources in flux-limited samples for $S \gtrsim 10$ mJy (Wilman et al. 2008; Padovani et al. 2011), and the median redshift for FRII sources is $z \approx 0.8$ with relatively small scatter (Condon 1988) such that a flux-limited sample may crudely approximate a volume-limited sample.

For a jet lying within an angle ϑ to the line of sight, the fraction of randomly-oriented sources pointed towards Earth is $1 - \cos(\vartheta)$. Orientation schemes predict that the transition from quasars (typically beamed) to radio galaxies (typically not beamed) is expected to occur at $\vartheta \sim 45^\circ$ (Barthel 1989; Urry & Padovani 1995). The critical angle to induce asymmetric depolarization in a double radio source (quasar or radio galaxy) is likely to be similar (e.g. Fernini 2001); here we estimate this angle as ranging between 30° and 70° , implying fractional surface densities of 15 – 65% amongst the general double radio source population. This is, of course, a crude model, not least because intracluster magnetic field

strengths at $z \sim 0.8$ (i.e. the expected median redshift for double radio sources; Condon 1988) are only expected to be a few percent of their $z = 0$ values (Dolag, Bartelmann, & Lesch 2002; Xu et al. 2009). A magnetised cluster atmosphere is clearly a prerequisite for depolarization, though a separate depolarizing medium close to the radio jets as described by Guidetti et al. (2012) may null this point.

As far as we are aware, no census of asymmetric depolarization has been performed for radio sources in a blind survey; studies to date have typically compiled samples of targeted observations (e.g. Fernini 2001; Kharb et al. 2008). The ATLAS data are suitable for this purpose. We note that it is difficult to estimate what the fractional surface density of asymmetrically depolarized sources might be if environmental asymmetries were to dominate, rather than orientation (significant merger activity is certainly expected in clusters; e.g. Tasitsiomi et al. 2004). Therefore, we simply focus on whether the ATLAS data are consistent with an orientation scheme or not.

To avoid selection effects relating to visibility area and the detectability of sources with low fractional polarization, we selected only the 40 ATLAS sources with total intensity $S > 30$ mJy. We expect that each of these sources is a radio-loud AGN with dual-lobe structure dominated by un-beamed lobe emission (though not all need exhibit multiple components due to viewing angle and source size). The breakdown of these 40 sources according to the polarization–total intensity classification scheme (see Section 1) is as follows. There was 1 polarized source classified as Type 3 (midway polarized), though it is unclear if this demonstrates a depolarization asymmetry or not. There were 7 polarized single-component sources classified as Type 4. In an attempt to account for the possibility that many of these ‘unclassified’ sources represent as-yet unassociated lobes of multi-component sources (see comments in Section 2.2), we assumed that perhaps only 1 of the detected Type 4 sources was likely to truly represent a polarized

single-component source. We have interpreted this as a dual-lobed asymmetrically-depolarized source with jet axis close to the line of sight, such that only a single component is effectively seen. There were 15 polarized dual-lobed sources classified as Type 6 (no asymmetric depolarization). There were 2 polarized dual-lobed sources classified as Type 7 (clear indication of asymmetric depolarization); for reference, these sources were displayed earlier in Fig. 17 of Paper I. There were 4 polarized dual-lobed sources classified as Type 8 (unclear whether asymmetrically depolarized or not). We assumed that approximately one quarter of these sources (i.e. 1 source) would likely demonstrate asymmetric depolarization if more sensitive observations were obtained. This assumption is consistent with the finding from Fig. 9 that most Type 8 sources have LASs reflective of Type 6 sources, rather than the smaller LASs observed for the Type 7 sources. Finally, our sample included 11 unpolarized sources (Type 9), each with fractional polarization upper limits below 1% (see Fig. 5). We do not interpret these sources as being asymmetrically depolarized.

We note that while it is possible that some of the 11 unpolarized sources represent unassociated lobes of multi-component sources, at least some of them must be truly isolated, single-component sources with $\Pi < 1\%$. For example, the brightest unpolarized source displayed in Fig. 5 is the source C3, which is barely-resolved in ATLAS DR2 (deconvolved angular size $1.69'' \pm 1.65''$) and has a 1.4 – 2.3 GHz spectral index of $\alpha = -0.4$ (Zinn et al. 2012). This source is therefore consistent with identification as a CSO (Readhead et al. 1996); CSOs are known to exhibit flat radio spectra (Augusto et al. 2006) and low fractional polarization due to strong depolarization (Cotton et al. 2003).

The statistics above suggest that between $1 + 2 + 1 = 4$ and $1 + 7 + 2 + 4 = 14$ of the 40 ATLAS DR2 sources in our flux density limited sample exhibit depolarization asymmetry, i.e., 10 – 35%. This fraction falls within the theoretical range estimated above, demonstrating that the Laing-Garrington effect appears consistent with orientation dependence, at least within the rudimentary confines of our analysis. Future high-resolution polarization studies are clearly required to form more robust conclusions.

4 CONCLUSIONS

In this work we have presented results and discussion for ATLAS DR2. Our key results are summarised as follows. For convenience we use the term ‘millijansky’ loosely below to indicate flux densities in the range 0.1 – 1000 mJy.

- (i) Radio emission from polarized millijansky sources is most likely powered by AGNs, where the active nuclei are embedded within host galaxies with mid-infrared spectra dominated by old-population (10 Gyr) starlight or continuum produced by dusty tori. We find no evidence for polarized SFGs or individual stars to the sensitivity limits of our data - all polarized ATLAS sources are classified as AGNs.
- (ii) The ATLAS data indicate that fractional polarization levels for sources with starlight-dominated mid-infrared hosts and those with continuum-dominated mid-infrared hosts are similar.
- (iii) The morphologies and angular sizes of polarized ATLAS components and sources are consistent with the interpretation that polarized emission in millijansky sources originates from the jets or lobes of extended AGNs, where coherent large-scale magnetic fields are likely to be present. We find that the majority of polarized ATLAS sources are resolved in total intensity, even though the majority of components in linear polarization are unresolved.

This is consistent with the interpretation that large-scale magnetic fields that do not completely beam depolarize are present in these sources, despite the relatively poor resolutions of the ATLAS data.

- (iv) We do not find any components or sources with fractional polarization levels greater than 24%, in contrast with previous studies of faint polarized sources. We attribute this finding to our improved data analysis procedures.
- (v) The ATLAS data are consistent with a distribution of fractional polarization at 1.4 GHz that is independent of flux density down to $I \sim 10$ mJy, and perhaps even down to 1 mJy when considering the upper envelope of the distribution. This result is in contrast to the findings from previous deep 1.4 GHz polarization surveys (with the very recent exception of Rudnick & Owen 2014), and is consistent with results at higher frequencies (≥ 4.8 GHz). The anti-correlation observed in previous 1.4 GHz studies is due to two effects: a selection bias, and spurious high fractional polarization detections. Both of these effects can become more prevalent at faint total flux densities. We find that components and sources can be characterised using the same distribution of fractional linear polarization, with a median level of 4%. We have presented a new lognormal model to describe the distribution of fractional polarization for 1.4 GHz components and sources, specific to AGNs, in surveys with resolution FWHMs $\sim 10''$.
- (vi) No polarized SFGs were detected in ATLAS DR2 down to the linear polarization detection threshold of $\sim 200 \mu\text{Jy}$. The ATLAS data constrain typical fractional polarization levels for the $I \gtrsim 100 \mu\text{Jy}$ SFG population to be $\Pi_{\text{SFG}} < 60\%$.
- (vii) Differences between differential number-counts of components and of sources in 1.4 GHz surveys with resolution FWHM $\sim 10''$ are not likely to be significant ($\lesssim 20\%$) at millijansky levels.
- (viii) The ATLAS total intensity differential source counts do not exhibit any unexpected flattening down to the survey limit $\sim 100 \mu\text{Jy}$.
- (ix) The ATLAS linearly polarized differential component counts do not exhibit any flattening below ~ 1 mJy, unlike previous findings which have led to suggestions of increasing levels of fractional polarization with decreasing flux density or the emergence of a new source population. The polarized counts down to $\sim 100 \mu\text{Jy}$ are consistent with being drawn from the total intensity counts at flux densities where luminous FR-type radio galaxies and quasars dominate.
- (x) Constrained by the ATLAS data, we estimate that the surface density of linearly polarized components in a 1.4 GHz survey with resolution FWHM $\sim 10''$ is 50 deg^{-2} for $L_{\text{comp}} \geq 100 \mu\text{Jy}$, and 90 deg^{-2} for $L_{\text{comp}} \geq 50 \mu\text{Jy}$. We estimate that the surface density for polarized sources is $\sim 45 \text{ deg}^{-2}$ for $L_{\text{src}} \geq 100 \mu\text{Jy}$, assuming that most polarized components belong to dual-component sources (e.g. FR-type) at these flux densities.
- (xi) We find that the statistics of ATLAS sources exhibiting asymmetric depolarization are consistent with the interpretation that the Laing-Garrington effect is due predominantly to source orientation within a surrounding magnetoionic medium. To our knowledge, this work represents the first attempt to investigate asymmetric depolarization in a blind survey.

ACKNOWLEDGMENTS

We thank Walter Max-Moerbeck for insightful discussions. We thank the anonymous referee for helpful comments that led to the improvement of this manuscript. C. A. H. acknowledges the support of an Australian Postgraduate Award, a CSIRO OCE Scholarship, and a Jansky Fellowship from the National Radio

Astronomy Observatory. B. M. G. and R. P. N. acknowledge the support of the Australian Research Council Centre of Excellence for All-sky Astrophysics (CAASTRO), through project number CE110001020. The Australia Telescope Compact Array is part of the Australia Telescope National Facility which is funded by the Commonwealth of Australia for operation as a National Facility managed by CSIRO. This paper includes archived data obtained through the Australia Telescope Online Archive (<http://atofa.atnf.csiro.au>).

REFERENCES

- Arshakian T. G., Beck R., 2011, *MNRAS*, 418, 2336
- Appleton P. N., et al., 2004, *ApJS*, 154, 147
- Augusto P., Gonzalez-Serrano J. I., Perez-Fournon I., Wilkinson P. N., 2006, *MNRAS*, 368, 1411
- Battye R. A., Browne I. W. A., Peel M. W., Jackson N. J., Dickinson C., 2011, *MNRAS*, 413, 132
- Banfield J. K., George S. J., Taylor A. R., Stil J. M., Kothes R., Scott D., 2011, *ApJ*, 733, 69
- Barthel P. D., 1989, *ApJ*, 336, 606
- Beck R., Gaensler B. M., 2004, *NewAR*, 48, 1289
- Bicknell G. V., Cameron R. A., Gingold R. A., 1990, *ApJ*, 357, 373
- Biggs A. D., Ivison R. J., 2006, *MNRAS*, 371, 963
- Blake C., Wall J., 2002, *MNRAS*, 337, 993
- Bondi M., et al., 2003, *A&A*, 403, 857
- Burn B. J., 1966, *MNRAS*, 133, 67
- Cales S. L., et al., 2011, *ApJ*, 741, 106
- Condon J. J., 2007, *ASPC*, 380, 189
- Condon J. J., et al., 2012, *ApJ*, 758, 23
- Condon J. J., Cotton W. D., Greisen E. W., Yin Q. F., Perley R. A., Taylor G. B., Broderick J. J., 1998, *AJ*, 115, 1693
- Condon J. J., 1988, *gera.book*, 641
- Cotton W. D., et al., 2003, *PASA*, 20, 12
- de Zotti G., Massardi M., Negrello M., Wall J., 2010, *A&ARv*, 18, 1
- Dolag K., Bartelmann M., Lesch H., 2002, *A&A*, 387, 383
- Dursi L. J., Frommer C., 2008, *ApJ*, 677, 993
- Ensslin T. A., Vogt C., Clarke T. E., Taylor G. B., 2003, *ApJ*, 597, 870
- Feain I. J., et al., 2009, *ApJ*, 707, 114
- Ferguson H. C., et al., 2004, *ApJ*, 600, L107
- Fernini I., 2001, *AJ*, 122, 83
- Fine S., Shanks T., Nikoloudakis N., Sawangwit U., 2011, *MNRAS*, 418, 2251
- Fixsen D. J., et al., 2011, *ApJ*, 734, 5
- Fomalont E. B., Kellermann K. I., Cowie L. L., Capak P., Barger A. J., Partridge R. B., Windhorst R. A., Richards E. A., 2006, *ApJS*, 167, 103
- Garrington S. T., Conway R. G., 1991, *MNRAS*, 250, 198
- Garrington S. T., Leahy J. P., Conway R. G., Laing R. A., 1988, *Natur*, 331, 147
- Gendre M. A., Wall J. V., 2008, *MNRAS*, 390, 819
- Ginzburg V. L., Syrovatskii S. I., 1965, *ARA&A*, 3, 297
- Gopal-Krishna, Wiita P. J., 2004, *arXiv:astro-ph/0409761*
- Grant J. K., Taylor A. R., Stil J. M., Landecker T. L., Kothes R., Ransom R. R., Scott D., 2010, *ApJ*, 714, 1689
- Guidetti D., Laing R. A., Bridle A. H., Parma P., Gregorini L., 2011, *MNRAS*, 413, 2525
- Guidetti D., Laing R. A., Croston J. H., Bridle A. H., Parma P., 2012, *MNRAS*, 423, 1335
- Hales C. A., Gaensler B. M., Norris R. P., Middelberg E., 2012a, *MNRAS*, 424, 2160
- Hales C. A., Murphy T., Curran J. R., Middelberg E., Gaensler B. M., Norris R. P., 2012b, *MNRAS*, 425, 979
- Hales C. A., et al., 2014 (Paper I), *MNRAS*, xxx, xxx
- Heywood I., Jarvis M. J., Condon J. J., 2013, *MNRAS*, 432, 2625
- Holder G. P., 2014, *ApJ*, 780, 112
- Hopkins A. M., Afonso J., Chan B., Cram L. E., Georgakakis A., Mobasher B., 2003, *AJ*, 125, 465
- Huarte-Espinosa M., Krause M., Alexander P., 2011, *MNRAS*, 418, 1621
- Ibar E., Ivison R. J., Biggs A. D., Lal D. V., Best P. N., Green D. A., 2009, *MNRAS*, 397, 281
- Ishwara-Chandra C. H., Saikia D. J., Kapahi V. K., McCarthy P. J., 1998, *MNRAS*, 300, 269
- Jarvis M. J., Rawlings S., 2004, *NewAR*, 48, 1173
- Johnson R. A., Leahy J. P., Garrington S. T., 1995, *MNRAS*, 273, 877
- Kaplan E. L., Meier P., 1958, *Journal of the American Statistical Association*, 53, 457
- Kashyap V. L., van Dyk D. A., Connors A., Freeman P. E., Siemiginowska A., Xu J., Zezas A., 2010, *ApJ*, 719, 900
- Kharb P., O'Dea C. P., Baum S. A., Daly R. A., Mory M. P., Donahue M., Guerra E. J., 2008, *ApJS*, 174, 74
- Kuchar P., Enßlin T. A., 2011, *A&A*, 529, A13
- Laing R. A., 1988, *Natur*, 331, 149
- Laing R. A., Bridle A. H., Parma P., Murgia M., 2008, *MNRAS*, 391, 521
- Lara L., Márquez I., Cotton W. D., Feretti L., Giovannini G., Marcaide J. M., Venturi T., 1999, *A&A*, 348, 699
- Liu R., Pooley G., 1991a, *MNRAS*, 249, 343
- Liu R., Pooley G., 1991b, *MNRAS*, 253, 669
- Lonsdale C. J., et al., 2003, *PASP*, 115, 897
- Mao M. Y., et al., 2012, *MNRAS*, 426, 3334
- Massardi M., Bonaldi A., Negrello M., Ricciardi S., Raccanelli A., de Zotti G., 2010, *MNRAS*, 404, 532
- Massardi M., et al., 2013, *MNRAS*, 436, 2915
- McCarthy P. J., van Breugel W., Kapahi V. K., 1991, *ApJ*, 371, 478
- Mesa D., Baccigalupi C., De Zotti G., Gregorini L., Mack K.-H., Vigotti M., Klein U., 2002, *A&A*, 396, 463
- Middelberg E., et al., 2008, *AJ*, 135, 1276
- Mitchell K. J., Condon J. J., 1985, *AJ*, 90, 1957
- Morrison G. E., Owen F. N., Dickinson M., Ivison R. J., Ibar E., 2010, *ApJS*, 188, 178
- Negrello M., Magliocchetti M., De Zotti G., 2006, *MNRAS*, 368, 935
- Nenkova M., Sirocky M. M., Ivezić Ž., Elitzur M., 2008, *ApJ*, 685, 147
- Norris R. P., et al., 2006, *AJ*, 132, 2409
- Norris R. P., Lenc E., Roy A. L., Spoon H., 2012, *MNRAS*, 422, 1453
- O'Dea C. P., 1998, *PASP*, 110, 493
- O'Sullivan S., Stil J., Taylor A. R., Ricci R., Grant J. K., Shorten K., 2008, in *POS, Proc. 9th Eur. VLBI Network Symp. for Radio Astron.*, p. 107
- O'Sullivan S. P., et al., 2013, *ApJ*, 764, 162
- Overzier R. A., Röttgering H. J. A., Rengelink R. B., Wilman R. J., 2003, *A&A*, 405, 53
- Owen F. N., Morrison G. E., 2008, *AJ*, 136, 1889

Padovani P., Miller N., Kellermann K. I., Mainieri V., Rosati P., Tozzi P., 2011, *ApJ*, 740, 20
 Pier E. A., Krolak J. H., 1993, *ApJ*, 418, 673
 Readhead A. C. S., Taylor G. B., Pearson T. J., Wilkinson P. N., 1996, *ApJ*, 460, 634
 Regener V. H., 1951, *Phys. Rev.*, 84, 161L
 Rudnick L., Blundell K. M., 2004, in Reiprich T., Kempner J., Soker N., eds, *Proc. of The Riddle of Cooling Flows in Galaxies and Clusters of Galaxies*, E37
 Rudnick L., Owen F. N., 2014, *ApJ*, in press (arXiv:1402.3637)
 Sajina A., Lacy M., Scott D., 2005, *ApJ*, 621, 256
 Sajina A., Partridge B., Evans T., Stefl S., Vechik N., Myers S., Dicker S., Korngut P., 2011, *ApJ*, 732, 45
 Sandage A., Lubin L. M., 2001, *AJ*, 121, 2271
 Scheuer P. A. G., 1957, *PCPS*, 53, 764
 Seiffert M., et al., 2011, *ApJ*, 734, 6
 Serkowski K., 1958, *AcA*, 8, 135
 Seymour N., McHardy I. M., Gunn K. F., 2004, *MNRAS*, 352, 131
 Shi H., Liang H., Han J. L., Hunstead R. W., 2010, *MNRAS*, 409, 821
 Simmons J. F. L., Stewart B. G., 1985, *A&A*, 142, 100
 Simpson C., et al., 2006, *MNRAS*, 372, 741
 Singal J., Stawarz Ł., Lawrence A., Petrosian V., 2010, *MNRAS*, 409, 1172
 Smolčić V., et al., 2008, *ApJS*, 177, 14
 Sokoloff D. D., Bykov A. A., Shukurov A., Berkhuijsen E. M., Beck R., Poezd A. D., 1998, *MNRAS*, 299, 189
 Stawarz Ł., et al., 2013, *ApJ*, 766, 48
 Stepanov R., Arshakian T. G., Beck R., Frick P., Krause M., 2008, *A&A*, 480, 45
 Stil J. M., Krause M., Beck R., Taylor A. R., 2009, *ApJ*, 693, 1392
 Subrahmanyam R., Ekers R. D., Saripalli L., Sadler E. M., 2010, *MNRAS*, 402, 2792
 Subrahmanyam R., Cowsik R., 2013, *ApJ*, 776, 42
 Tasitsiomi A., Kravtsov A. V., Gottlöber S., Klypin A. A., 2004, *ApJ*, 607, 125
 Taylor A. R., et al., 2007, *ApJ*, 666, 201
 Thorat K., Subrahmanyam R., Saripalli L., Ekers R. D., 2013, *ApJ*, 762, 16
 Tolman R. C., 1930, *PNAS*, 16, 511
 Tribble P. C., 1992, *MNRAS*, 256, 281
 Tribble P. C., 1991, *MNRAS*, 250, 726
 Tucci M., Martínez-González E., Toffolatti L., González-Nuevo J., De Zotti G., 2004, *MNRAS*, 349, 1267
 Tucci M., Toffolatti L., 2012, *AdAst*, 2012, 624987
 Urry C. M., Padovani P., 1995, *PASP*, 107, 803
 van der Marel R. P., Franx M., 1993, *ApJ*, 407, 525
 Vernstrom T., Scott D., Wall J. V., 2011, *MNRAS*, 415, 3641
 White R. L., Becker R. H., Helfand D. J., Gregg M. D., 1997, *ApJ*, 475, 479
 Wilman R. J., et al., 2008, *MNRAS*, 388, 1335
 Windhorst R. A., van Heerde G. M., Katgert P., 1984, *A&AS*, 58, 1
 Wright E. L., 2006, *PASP*, 118, 1711
 Xu H., Li H., Collins D. C., Li S., Norman M. L., 2009, *ApJ*, 698, L14
 Zinn P.-C., Middelberg E., Norris R. P., Hales C. A., Mao M. Y., Randall K. E., 2012, *A&A*, 544, A38

APPENDIX A: DIFFERENTIAL COMPONENT COUNTS

This appendix presents 1.4 GHz Euclidean-normalised differential number-counts, in tabulated form, derived from the ATLAS DR2 total intensity and linear polarization component catalogues from Appendix A of Paper I.

The tabulated results have been organised as follows according to emission type, Eddington bias correction scheme, and ATLAS field. Tables A1 and A2 (each with 7 columns) present total intensity number-counts for the CDF-S and ELAIS-S1 fields, respectively, using ‘component-corrected’ data whereby individual components were deboosted prior to the application of visibility area and resolution bias corrections. Similarly, Tables A3 and A4 (each with 9 columns) present total intensity number-counts for the two ATLAS fields, but now using ‘bin-corrected’ data whereby non-deboosted components were corrected for visibility area, resolution bias, and Eddington bias. Tables A5 and A6 (each with 11 columns) present linear polarization number-counts for the CDF-S and ELAIS-S1 fields, respectively, using component-corrected data. Tables A7 and A8 (each with 17 columns) present bin-corrected linear polarization number-counts for the CDF-S and ELAIS-S1 fields, respectively.

Columns for the tables above are organised as follows. Tables describing component-corrected total intensity data give for each bin the flux density range (ΔS), expected average flux density (S_{AV}), raw number of deboosted components (N_{raw}^D), effective number of deboosted components following visibility area correction only (N_{eff}^{DV}), effective number of deboosted components following both visibility area and resolution bias corrections (N_{eff}^{DVR}), Euclidean-normalised counts following visibility area correction only ($S^{2.5} dN_{eff}^{DV} / dS$), and Euclidean-normalised counts following both visibility area and resolution bias corrections ($S^{2.5} dN_{eff}^{DVR} / dS$). Columns for tables describing bin-corrected total intensity data are similar, but without the superscript D which indicates use of deboosted component data. The bin-corrected tables contain two additional columns: effective number of components following combined visibility area, resolution bias, and Eddington bias corrections (N_{eff}^{VRE}), and an associated column for their Euclidean-normalised counts ($S^{2.5} dN_{eff}^{VRE} / dS$). The tables describing linear polarization data are similar to those for total intensity data, but with additional columns cataloguing the effective number of components or Euclidean-normalised counts resulting from the resolution bias corrections associated with the lower (-R) or upper (+R) bounds described in Section 7.1 of Paper I and displayed in Fig. 22 of Paper I. Thus the additional columns have been assigned descriptors with superscripts V-R, V+R, V-RE, and V+RE. Errors associated with the fully corrected Euclidean-normalised counts in the figures and tables above are 1σ Poissonian and were calculated following Regener (1951).

This paper has been typeset from a \LaTeX file prepared by the author.

Table A1. ATLAS 1.4 GHz DR2 total intensity component-corrected counts for CDF-S field. See Appendix A for column details.

ΔI (mJy) (1)	I_{AV} (mJy) (2)	N_{raw}^D (3)	N_{eff}^{DV} (4)	N_{eff}^{DVR} (5)	$I^{2.5} dN_{\text{eff}}^{DV} / dI$ (Jy ^{1.5} sr ⁻¹) (6)	$I^{2.5} dN_{\text{eff}}^{DVR} / dI$ (Jy ^{1.5} sr ⁻¹) (7)
0.159 – 0.187	0.172	66	309.5	367.9	3.93	4.67 ^{+0.57} _{-0.57}
0.187 – 0.219	0.202	98	214.0	232.2	3.46	3.75 ^{+0.38} _{-0.38}
0.219 – 0.258	0.238	125	198.6	228.3	4.08	4.70 ^{+0.42} _{-0.42}
0.258 – 0.303	0.279	118	162.0	204.7	4.24	5.36 ^{+0.49} _{-0.49}
0.303 – 0.356	0.328	94	115.9	156.7	3.86	5.23 ^{+0.54} _{-0.54}
0.356 – 0.418	0.386	89	99.6	141.9	4.23	6.03 ^{+0.64} _{-0.64}
0.418 – 0.491	0.453	82	86.1	125.4	4.66	6.78 ^{+0.75} _{-0.75}
0.491 – 0.577	0.532	77	77.5	110.0	5.34	7.58 ^{+0.86} _{-0.86}
0.577 – 0.678	0.626	38	38.0	52.0	3.34	4.57 ^{+0.87} _{-0.74}
0.678 – 0.797	0.735	40	41.5	54.8	4.65	6.13 ^{+1.1} _{-0.97}
0.797 – 0.936	0.864	43	43.2	55.0	6.15	7.84 ^{+1.4} _{-1.2}
0.936 – 1.10	1.01	26	26.7	32.9	4.85	5.98 ^{+1.4} _{-1.2}
1.10 – 1.48	1.28	66	66.4	78.6	9.15	10.8 ^{+1.3} _{-1.3}
1.48 – 2.00	1.72	49	49.3	55.8	10.6	12.0 ^{+2.0} _{-1.7}
2.00 – 2.70	2.33	45	45.0	49.2	15.2	16.6 ^{+2.9} _{-2.5}
2.70 – 3.64	3.14	32	32.0	34.1	17.0	18.1 ^{+3.8} _{-3.2}
3.64 – 4.91	4.24	33	33.0	34.5	27.4	28.7 ^{+5.9} _{-5.0}
4.91 – 6.63	5.71	20	20.0	20.6	26.1	26.9 ^{+7.5} _{-6.0}
6.63 – 8.94	7.71	15	15.0	15.3	30.6	31.3 ⁺¹⁰ _{-8.0}
8.94 – 12.1	10.4	17	17.0	17.2	54.4	55.2 ⁺¹⁷ ₋₁₃
12.1 – 19.1	15.2	20	20.0	20.2	73.5	74.2 ⁺²¹ ₋₁₆
19.1 – 30.3	24.1	15	15.0	15.1	110	110 ⁺³⁶ ₋₂₈
30.3 – 48.0	38.2	9	9.0	9.0	131	132 ⁺⁶⁰ ₋₄₃
48.0 – 76.1	60.5	6	6.0	6.0	174	175 ⁺¹⁰⁰ ₋₆₉
76.1 – 121	95.9	6	6.0	6.0	347	348 ⁺²¹⁰ ₋₁₄₀
121 – 191	152	1	1.0	1.0	115	115 ⁺²⁷⁰ ₋₉₅
191 – 303	240	2	2.0	2.0	459	459 ⁺⁶¹⁰ ₋₃₀₀
761 – 1206	952	1	1.0	1.0	1800	1800 ⁺⁴¹⁰⁰ ₋₁₅₀₀

Table A2. ATLAS 1.4 GHz DR2 total intensity component-corrected counts for ELAIS-S1 field. See Appendix A for column details.

ΔI (mJy) (1)	I_{AV} (mJy) (2)	N_{raw}^D (3)	N_{eff}^{DV} (4)	N_{eff}^{DVR} (5)	$I^{2.5} dN_{\text{eff}}^{DV} / dI$ (Jy ^{1.5} sr ⁻¹) (6)	$I^{2.5} dN_{\text{eff}}^{DVR} / dI$ (Jy ^{1.5} sr ⁻¹) (7)
0.139 – 0.163	0.151	88	245.9	256.4	3.34	3.49 ^{+0.37} _{-0.37}
0.163 – 0.192	0.177	108	208.2	221.0	3.60	3.82 ^{+0.37} _{-0.37}
0.192 – 0.225	0.208	109	169.6	200.5	3.74	4.42 ^{+0.42} _{-0.42}
0.225 – 0.265	0.244	108	147.0	189.3	4.13	5.31 ^{+0.51} _{-0.51}
0.265 – 0.311	0.287	71	86.5	118.5	3.09	4.24 ^{+0.50} _{-0.50}
0.311 – 0.366	0.337	85	94.7	135.9	4.31	6.18 ^{+0.67} _{-0.67}
0.366 – 0.430	0.396	68	71.6	103.1	4.15	5.98 ^{+0.72} _{-0.72}
0.430 – 0.505	0.465	60	61.1	85.9	4.51	6.34 ^{+0.82} _{-0.82}
0.505 – 0.593	0.547	50	50.2	68.4	4.73	6.44 ^{+1.0} _{-0.91}
0.593 – 0.697	0.643	51	51.8	68.2	6.21	8.17 ^{+1.1} _{-1.1}
0.697 – 0.818	0.755	29	29.9	38.0	4.56	5.80 ^{+1.3} _{-1.1}
0.818 – 0.962	0.887	37	38.0	46.8	7.39	9.10 ^{+1.8} _{-1.5}
0.962 – 1.13	1.04	22	22.8	27.2	5.64	6.74 ^{+1.8} _{-1.4}
1.13 – 1.52	1.31	35	35.9	41.3	6.75	7.77 ^{+1.5} _{-1.3}
1.52 – 2.06	1.77	46	46.4	51.3	13.7	15.1 ^{+2.6} _{-2.2}
2.06 – 2.77	2.39	29	29.1	31.2	13.4	14.4 ^{+3.2} _{-2.7}
2.77 – 3.74	3.22	25	25.0	26.3	18.1	19.0 ^{+4.6} _{-3.8}
3.74 – 5.05	4.35	26	26.4	27.3	29.9	31.0 ^{+7.4} _{-6.0}
5.05 – 6.81	5.87	20	20.2	20.7	35.9	36.8 ⁺¹⁰ _{-8.1}
6.81 – 9.18	7.92	20	20.0	20.4	55.7	56.7 ⁺¹⁶ ₋₁₃
9.18 – 12.4	10.7	11	11.2	11.4	49.1	49.6 ⁺²⁰ ₋₁₅
12.4 – 19.6	15.6	9	9.0	9.1	45.1	45.5 ⁺²¹ ₋₁₅
19.6 – 31.1	24.8	12	12.0	12.0	120	120 ⁺⁴⁶ ₋₃₄
31.1 – 49.3	39.2	5	5.0	5.0	99.5	99.7 ⁺⁶⁷ ₋₄₃
49.3 – 78.2	62.2	5	5.0	5.0	198	198 ⁺¹³⁰ ₋₈₆
124 – 196	156	2	2.0	2.0	315	315 ⁺⁴²⁰ ₋₂₀₀

Table A3. ATLAS 1.4 GHz DR2 total intensity bin-corrected counts for CDF-S field. See Appendix A for column details.

ΔI (mJy) (1)	I_{AV} (mJy) (2)	N_{raw} (3)	$N_{\text{eff}}^{\text{V}}$ (4)	$N_{\text{eff}}^{\text{VR}}$ (5)	$N_{\text{eff}}^{\text{VRE}}$ (6)	$I^{2.5} dN_{\text{eff}}^{\text{V}}/dI$ (Jy ^{1.5} sr ⁻¹) (7)	$I^{2.5} dN_{\text{eff}}^{\text{VR}}/dI$ (Jy ^{1.5} sr ⁻¹) (8)	$I^{2.5} dN_{\text{eff}}^{\text{VRE}}/dI$ (Jy ^{1.5} sr ⁻¹) (9)
0.169 – 0.199	0.183	59	334.9	396.2	265.7	4.65	5.51	3.69 ^{+0.48} _{-0.48}
0.199 – 0.233	0.215	96	232.1	251.8	178.4	4.11	4.46	3.16 ^{+0.32} _{-0.32}
0.233 – 0.274	0.253	146	234.6	280.8	216.5	5.29	6.33	4.88 ^{+0.40} _{-0.40}
0.274 – 0.322	0.297	123	167.9	218.3	180.3	4.82	6.27	5.17 ^{+0.47} _{-0.47}
0.322 – 0.378	0.349	94	114.8	158.6	140.5	4.20	5.80	5.14 ^{+0.53} _{-0.53}
0.378 – 0.445	0.410	96	106.4	153.7	141.6	4.95	7.16	6.59 ^{+0.67} _{-0.67}
0.445 – 0.522	0.482	79	82.1	118.5	112.6	4.87	7.03	6.68 ^{+0.75} _{-0.75}
0.522 – 0.614	0.566	76	76.3	106.9	103.2	5.76	8.08	7.79 ^{+0.89} _{-0.89}
0.614 – 0.721	0.665	43	43.3	58.5	57.1	4.17	5.63	5.49 ^{+0.97} _{-0.83}
0.721 – 0.847	0.781	36	37.2	48.5	47.7	4.56	5.94	5.84 ^{+1.1} _{-0.97}
0.847 – 0.995	0.918	40	40.2	50.6	50.0	6.28	7.90	7.81 ^{+1.4} _{-1.2}
0.995 – 1.17	1.08	29	29.7	36.2	35.9	5.90	7.20	7.14 ^{+1.6} _{-1.3}
1.17 – 1.58	1.36	61	61.4	71.9	71.6	9.27	10.9	10.8 ^{+1.4} _{-1.4}
1.58 – 2.13	1.83	53	53.3	59.8	59.6	12.6	14.2	14.1 ^{+1.9} _{-1.9}
2.13 – 2.87	2.47	43	43.0	46.7	46.7	16.0	17.3	17.3 ^{+3.1} _{-2.6}
2.87 – 3.87	3.34	30	30.0	31.8	31.8	17.4	18.5	18.5 ^{+4.0} _{-3.4}
3.87 – 5.22	4.50	31	31.0	32.3	32.3	28.3	29.4	29.5 ^{+6.3} _{-5.3}
5.22 – 7.05	6.07	17	17.0	17.5	17.5	24.3	25.0	25.0 ^{+7.6} _{-6.0}
7.05 – 9.50	8.19	16	16.0	16.3	16.3	35.8	36.6	36.6 ⁺¹² _{-9.0}
9.50 – 12.8	11.1	18	18.0	18.3	18.3	63.1	64.0	64.0 ⁺¹⁹ ₋₁₅
12.8 – 20.3	16.2	18	18.0	18.2	18.2	72.4	73.2	73.1 ⁺²² ₋₁₇
20.3 – 32.2	25.6	16	16.0	16.1	16.1	128	129	129 ⁺⁴¹ ₋₃₂
32.2 – 51.0	40.6	8	8.0	8.0	8.0	128	128	128 ⁺⁶³ ₋₄₄
51.0 – 80.9	64.3	5	5.0	5.0	5.0	159	161	161 ⁺¹¹⁰ ₋₆₉
80.9 – 128	102	5	5.0	5.0	5.0	317	317	317 ⁺²¹⁰ ₋₁₄₀
128 – 203	161	1	1.0	1.0	1.0	126	126	126 ⁺²⁹⁰ ₋₁₀₀
203 – 322	256	2	2.0	2.0	2.0	503	503	503 ⁺⁶⁶⁰ ₋₃₃₀
809 – 1282	1012	1	1.0	1.0	1.0	1970	1970	1970 ⁺⁴⁵⁰⁰ ₋₁₆₀₀

Table A4. ATLAS 1.4 GHz DR2 total intensity bin-corrected counts for ELAIS-S1 field. See Appendix A for column details.

ΔI (mJy) (1)	I_{AV} (mJy) (2)	N_{raw} (3)	N_{eff}^V (4)	N_{eff}^{VR} (5)	N_{eff}^{VRE} (6)	$I^{2.5} dN_{eff}^V / dI$ (Jy ^{1.5} sr ⁻¹) (7)	$I^{2.5} dN_{eff}^{VR} / dI$ (Jy ^{1.5} sr ⁻¹) (8)	$I^{2.5} dN_{eff}^{VRE} / dI$ (Jy ^{1.5} sr ⁻¹) (9)
0.149 – 0.175	0.161	90	286.2	289.1	206.9	4.32	4.36	3.12 ^{+0.33} _{-0.33}
0.175 – 0.206	0.190	117	229.5	254.0	189.2	4.41	4.88	3.63 ^{+0.34} _{-0.34}
0.206 – 0.242	0.223	116	179.9	221.6	173.8	4.40	5.42	4.25 ^{+0.39} _{-0.39}
0.242 – 0.284	0.262	116	156.0	206.7	173.6	4.86	6.44	5.41 ^{+0.50} _{-0.50}
0.284 – 0.334	0.308	76	90.6	126.8	111.9	3.59	5.03	4.44 ^{+0.51} _{-0.51}
0.334 – 0.392	0.361	81	88.9	129.1	119.3	4.49	6.53	6.03 ^{+0.67} _{-0.67}
0.392 – 0.460	0.425	68	70.9	101.0	95.7	4.56	6.50	6.16 ^{+0.75} _{-0.75}
0.460 – 0.541	0.499	64	64.9	90.0	86.9	5.32	7.37	7.13 ^{+0.75} _{-0.89}
0.541 – 0.636	0.586	50	50.3	67.6	66.0	5.25	7.06	6.89 ^{+1.1} _{-0.97}
0.636 – 0.747	0.689	43	44.5	57.7	56.7	5.92	7.67	7.54 ^{+1.3} _{-1.1}
0.747 – 0.877	0.809	36	36.0	45.2	44.6	6.10	7.65	7.56 ^{+1.5} _{-1.3}
0.877 – 1.03	0.951	31	32.0	38.9	38.6	6.90	8.38	8.32 ^{+1.8} _{-1.5}
1.03 – 1.39	1.20	34	34.9	40.7	40.6	5.71	6.67	6.64 ^{+1.3} _{-1.1}
1.39 – 1.88	1.62	39	40.1	44.9	44.8	10.3	11.5	11.5 ^{+2.2} _{-1.8}
1.88 – 2.53	2.18	41	41.0	44.4	44.4	16.5	17.9	17.9 ^{+3.2} _{-2.8}
2.53 – 3.41	2.94	25	25.1	26.5	26.5	15.8	16.7	16.7 ^{+4.1} _{-3.3}
3.41 – 4.60	3.97	23	23.4	24.3	24.3	23.1	24.0	24.0 ^{+6.1} _{-5.0}
4.60 – 6.21	5.36	25	25.2	25.8	25.8	39.0	40.1	40.0 ^{+9.7} _{-7.9}
6.21 – 8.38	7.22	18	18.0	18.3	18.3	43.7	44.5	44.5 ⁺¹³ ₋₁₀
8.38 – 11.3	9.74	15	15.2	15.4	15.4	58.0	58.7	58.6 ⁺¹⁹ ₋₁₅
11.3 – 17.9	14.3	10	10.0	10.1	10.1	43.7	44.0	44.0 ⁺¹⁹ ₋₁₄
17.9 – 28.4	22.6	13	13.0	13.0	13.1	113	114	114 ⁺⁴¹ ₋₃₁
28.4 – 45.0	35.8	4	4.0	4.0	4.0	69.4	69.5	69.5 ⁺⁵⁵ ₋₃₃
45.0 – 71.3	56.7	4	4.0	4.0	4.0	138	138	138 ⁺¹¹⁰ ₋₆₆
71.3 – 113	89.9	2	2.0	2.0	2.0	138	138	138 ⁺¹⁸⁰ ₋₈₉
113 – 179	142	2	2.0	2.0	2.0	274	274	274 ⁺³⁶⁰ ₋₁₈₀

Table A5. ATLAS 1.4 GHz DR2 linear polarization component-corrected counts for CDF-S field. See Appendix A for column details.

ΔL (mJy) (1)	L_{AV} (mJy) (2)	N_{raw}^D (3)	N_{eff}^{DV} (4)	N_{eff}^{DV-R} (5)	N_{eff}^{DVR} (6)	N_{eff}^{DV+R} (7)	$L^{2.5} dN_{eff}^{DV} / dL$ (Jy ^{1.5} sr ⁻¹) (8)	$L^{2.5} dN_{eff}^{DV-R} / dL$ (Jy ^{1.5} sr ⁻¹) (9)	$L^{2.5} dN_{eff}^{DVR} / dL$ (Jy ^{1.5} sr ⁻¹) (10)	$L^{2.5} dN_{eff}^{DV+R} / dL$ (Jy ^{1.5} sr ⁻¹) (11)
0.120 – 0.173	0.144	18	40.1	39.9	42.1	44.6	0.170	0.170 ^{+0.050} _{-0.040}	0.179 ^{+0.053} _{-0.042}	0.189 ^{+0.056} _{-0.044}
0.173 – 0.251	0.209	18	23.8	29.3	31.9	34.3	0.175	0.216 ^{+0.064} _{-0.050}	0.236 ^{+0.070} _{-0.055}	0.253 ^{+0.075} _{-0.059}
0.251 – 0.362	0.302	24	26.6	35.0	38.3	41.2	0.341	0.449 ^{+0.11} _{-0.091}	0.491 ^{+0.12} _{-0.100}	0.529 ^{+0.13} _{-0.11}
0.362 – 0.524	0.436	13	13.5	17.1	18.2	19.2	0.302	0.383 ^{+0.14} _{-0.10}	0.407 ^{+0.15} _{-0.11}	0.428 ^{+0.15} _{-0.12}
0.524 – 0.757	0.631	15	15.8	18.9	19.6	20.3	0.613	0.734 ^{+0.24} _{-0.19}	0.761 ^{+0.25} _{-0.19}	0.788 ^{+0.26} _{-0.20}
0.757 – 1.09	0.912	7	7.0	8.0	8.2	8.4	0.475	0.541 ^{+0.29} _{-0.20}	0.553 ^{+0.30} _{-0.20}	0.568 ^{+0.31} _{-0.21}
1.09 – 1.58	1.32	6	6.0	6.6	6.7	6.8	0.702	0.768 ^{+0.46} _{-0.30}	0.781 ^{+0.47} _{-0.31}	0.798 ^{+0.48} _{-0.32}
1.58 – 2.29	1.90	5	5.0	5.3	5.4	5.5	1.02	1.08 ^{+0.73} _{-0.47}	1.09 ^{+0.74} _{-0.47}	1.11 ^{+0.75} _{-0.48}
2.29 – 3.31	2.75	2	2.0	2.1	2.1	2.1	0.706	0.735 ^{+0.97} _{-0.47}	0.743 ^{+0.98} _{-0.48}	0.755 ^{+1.00} _{-0.49}
4.78 – 6.91	5.75	1	1.0	1.0	1.0	1.0	1.06	1.08 ^{+2.5} _{-0.90}	1.09 ^{+2.5} _{-0.90}	1.10 ^{+2.5} _{-0.91}
9.98 – 14.4	12.0	2	2.0	2.0	2.0	2.0	6.42	6.48 ^{+8.5} _{-4.2}	6.51 ^{+8.6} _{-4.2}	6.57 ^{+8.7} _{-4.2}
14.4 – 28.8	20.3	1	1.0	1.0	1.0	1.0	3.71	3.72 ^{+8.6} _{-3.1}	3.74 ^{+8.6} _{-3.1}	3.77 ^{+8.7} _{-3.1}
28.8 – 57.4	40.4	1	1.0	1.0	1.0	1.0	10.4	10.4 ⁺²⁴ _{-8.6}	10.4 ⁺²⁴ _{-8.6}	10.5 ⁺²⁴ _{-8.7}

Table A6. ATLAS 1.4 GHz DR2 linear polarization component-corrected counts for ELAIS-S1 field. See Appendix A for column details.

ΔL (mJy) (1)	L_{AV} (mJy) (2)	N_{raw}^D (3)	N_{eff}^{DV} (4)	N_{eff}^{DV-R} (5)	N_{eff}^{DVR} (6)	N_{eff}^{DV+R} (7)	$L^{2.5} dN_{eff}^{DV}/dL$ (Jy ^{1.5} sr ⁻¹) (8)	$L^{2.5} dN_{eff}^{DV-R}/dL$ (Jy ^{1.5} sr ⁻¹) (9)	$L^{2.5} dN_{eff}^{DVR}/dL$ (Jy ^{1.5} sr ⁻¹) (10)	$L^{2.5} dN_{eff}^{DV+R}/dL$ (Jy ^{1.5} sr ⁻¹) (11)
0.135 – 0.195	0.162	11	25.1	24.5	26.1	27.7	0.167	$0.163^{+0.065}_{-0.048}$	$0.173^{+0.070}_{-0.051}$	$0.184^{+0.074}_{-0.055}$
0.195 – 0.282	0.235	13	17.7	22.4	24.5	26.5	0.205	$0.259^{+0.093}_{-0.071}$	$0.284^{+0.10}_{-0.078}$	$0.307^{+0.11}_{-0.084}$
0.282 – 0.408	0.340	7	7.9	10.6	11.7	12.6	0.158	$0.213^{+0.11}_{-0.079}$	$0.234^{+0.13}_{-0.086}$	$0.253^{+0.14}_{-0.093}$
0.408 – 0.589	0.491	6	6.4	8.2	8.8	9.3	0.222	$0.288^{+0.17}_{-0.11}$	$0.307^{+0.18}_{-0.12}$	$0.325^{+0.19}_{-0.13}$
0.589 – 0.852	0.710	8	8.0	9.7	10.1	10.6	0.485	$0.590^{+0.29}_{-0.20}$	$0.615^{+0.30}_{-0.21}$	$0.640^{+0.32}_{-0.22}$
0.852 – 1.23	1.03	2	2.4	2.8	2.8	2.9	0.254	$0.292^{+0.38}_{-0.19}$	$0.300^{+0.40}_{-0.19}$	$0.310^{+0.41}_{-0.20}$
1.23 – 1.78	1.48	4	4.0	4.4	4.5	4.6	0.732	$0.807^{+0.64}_{-0.39}$	$0.824^{+0.65}_{-0.39}$	$0.846^{+0.67}_{-0.40}$
1.78 – 2.57	2.14	4	4.0	4.3	4.3	4.4	1.27	$1.36^{+1.1}_{-0.65}$	$1.38^{+1.1}_{-0.66}$	$1.41^{+1.1}_{-0.68}$
2.57 – 3.72	3.10	2	2.0	2.1	2.1	2.2	1.10	$1.15^{+1.5}_{-0.75}$	$1.17^{+1.5}_{-0.76}$	$1.20^{+1.6}_{-0.77}$
3.72 – 5.37	4.47	1	1.0	1.0	1.0	1.1	0.959	$0.987^{+2.3}_{-0.82}$	$1.000^{+2.3}_{-0.83}$	$1.02^{+2.3}_{-0.84}$
5.37 – 7.77	6.46	1	1.0	1.0	1.0	1.0	1.67	$1.70^{+3.9}_{-1.4}$	$1.71^{+3.9}_{-1.4}$	$1.74^{+4.0}_{-1.4}$

Table A7. ATLAS 1.4 GHz DR2 linear polarization bin-corrected counts for CDF-S field – Part I of II. See Appendix A for column details.

ΔL (mJy) (1)	L_{AV} (mJy) (2)	N_{raw} (3)	N_{eff}^V (4)	N_{eff}^{V-R} (5)	N_{eff}^{VR} (6)	N_{eff}^{V+R} (7)	N_{eff}^{V-RE} (8)	N_{eff}^{VRE} (9)	N_{eff}^{V+RE} (10)	$L^{2.5} dN_{eff}^V/dL$ (Jy ^{1.5} sr ⁻¹) (11)
0.125 – 0.181	0.150	18	40.1	40.2	42.3	44.6	39.4	41.5	43.7	0.181
0.181 – 0.261	0.218	18	23.8	29.8	32.6	35.1	29.1	31.8	34.3	0.187
0.261 – 0.377	0.315	24	26.6	34.9	38.0	40.8	34.4	37.5	40.3	0.363
0.377 – 0.546	0.455	15	16.3	20.5	21.8	22.9	20.4	21.6	22.7	0.387
0.546 – 0.789	0.657	14	14.0	16.7	17.3	17.9	16.6	17.2	17.8	0.578
0.789 – 1.14	0.950	6	6.0	6.9	7.0	7.2	6.8	7.0	7.2	0.433
1.14 – 1.65	1.37	6	6.0	6.5	6.6	6.8	6.5	6.6	6.8	0.747
1.65 – 2.38	1.98	5	5.0	5.3	5.4	5.5	5.3	5.4	5.5	1.08
2.38 – 3.44	2.87	2	2.0	2.1	2.1	2.1	2.1	2.1	2.1	0.751
4.98 – 7.19	5.99	1	1.0	1.0	1.0	1.0	1.0	1.0	1.0	1.13
10.4 – 20.7	14.7	3	3.0	3.0	3.0	3.1	3.0	3.0	3.1	6.83
41.4 – 82.6	57.9	1	1.0	1.0	1.0	1.0	1.0	1.0	1.0	17.7

Table A7 – continued ATLAS 1.4 GHz DR2 linear polarization bin-corrected counts for CDF-S field – Part II of II. See Appendix A for column details.

$L^{2.5} dN_{eff}^{V-R}/dL$ (Jy ^{1.5} sr ⁻¹) (12)	$L^{2.5} dN_{eff}^{VR}/dL$ (Jy ^{1.5} sr ⁻¹) (13)	$L^{2.5} dN_{eff}^{V+R}/dL$ (Jy ^{1.5} sr ⁻¹) (14)	$L^{2.5} dN_{eff}^{V-RE}/dL$ (Jy ^{1.5} sr ⁻¹) (15)	$L^{2.5} dN_{eff}^{VRE}/dL$ (Jy ^{1.5} sr ⁻¹) (16)	$L^{2.5} dN_{eff}^{V+RE}/dL$ (Jy ^{1.5} sr ⁻¹) (17)
0.182	0.191	0.201	$0.178^{+0.053}_{-0.042}$	$0.187^{+0.055}_{-0.044}$	$0.197^{+0.058}_{-0.046}$
0.234	0.256	0.276	$0.228^{+0.068}_{-0.053}$	$0.250^{+0.074}_{-0.058}$	$0.269^{+0.080}_{-0.063}$
0.476	0.519	0.557	$0.469^{+0.12}_{-0.095}$	$0.512^{+0.13}_{-0.10}$	$0.550^{+0.14}_{-0.11}$
0.488	0.517	0.543	$0.484^{+0.16}_{-0.12}$	$0.513^{+0.17}_{-0.13}$	$0.539^{+0.18}_{-0.14}$
0.687	0.712	0.736	$0.686^{+0.24}_{-0.18}$	$0.710^{+0.25}_{-0.19}$	$0.735^{+0.25}_{-0.19}$
0.491	0.502	0.515	$0.490^{+0.29}_{-0.19}$	$0.501^{+0.30}_{-0.20}$	$0.514^{+0.31}_{-0.20}$
0.814	0.827	0.844	$0.812^{+0.49}_{-0.32}$	$0.825^{+0.49}_{-0.33}$	$0.843^{+0.50}_{-0.33}$
1.15	1.16	1.18	$1.15^{+0.78}_{-0.50}$	$1.16^{+0.79}_{-0.50}$	$1.18^{+0.80}_{-0.51}$
0.779	0.788	0.800	$0.779^{+1.0}_{-0.50}$	$0.787^{+1.0}_{-0.51}$	$0.800^{+1.1}_{-0.52}$
1.15	1.16	1.17	$1.15^{+2.6}_{-0.95}$	$1.16^{+2.7}_{-0.96}$	$1.17^{+2.7}_{-0.97}$
6.86	6.90	6.96	$6.86^{+6.7}_{-3.7}$	$6.89^{+6.7}_{-3.8}$	$6.96^{+6.8}_{-3.8}$
17.7	17.8	17.9	17.7^{+41}_{-15}	17.8^{+41}_{-15}	17.9^{+41}_{-15}

Table A8. ATLAS 1.4 GHz DR2 linear polarization bin-corrected counts for ELAIS-S1 field – Part I of II. See Appendix A for column details.

ΔL (mJy) (1)	L_{AV} (mJy) (2)	N_{raw} (3)	N_{eff}^V (4)	N_{eff}^{V-R} (5)	N_{eff}^{VR} (6)	N_{eff}^{V+R} (7)	N_{eff}^{V-RE} (8)	N_{eff}^{VRE} (9)	N_{eff}^{V+RE} (10)	$L^{2.5} dN_{eff}^V / dL$ (Jy ^{1.5} sr ⁻¹) (11)
0.145 – 0.210	0.175	11	25.1	25.8	27.4	29.0	25.5	27.0	28.7	0.186
0.210 – 0.303	0.252	14	19.0	24.7	27.2	29.5	24.1	26.6	28.8	0.244
0.303 – 0.438	0.365	7	7.7	10.3	11.2	12.1	10.1	11.1	11.9	0.172
0.438 – 0.633	0.527	6	6.3	8.1	8.6	9.1	8.0	8.6	9.0	0.246
0.633 – 0.915	0.762	7	7.0	8.4	8.7	9.1	8.4	8.7	9.0	0.473
0.915 – 1.32	1.10	2	2.4	2.7	2.8	2.9	2.7	2.8	2.9	0.282
1.32 – 1.91	1.59	5	5.0	5.5	5.6	5.7	5.5	5.6	5.7	1.02
1.91 – 2.76	2.30	4	4.0	4.3	4.3	4.4	4.2	4.3	4.4	1.42
2.76 – 3.99	3.32	2	2.0	2.1	2.1	2.2	2.1	2.1	2.2	1.23
3.99 – 5.77	4.80	1	1.0	1.0	1.0	1.1	1.0	1.0	1.1	1.07

Table A8 – continued ATLAS 1.4 GHz DR2 linear polarization bin-corrected counts for ELAIS-S1 field – Part II of II. See Appendix A for column details.

$L^{2.5} dN_{eff}^{V-R} / dL$ (Jy ^{1.5} sr ⁻¹) (12)	$L^{2.5} dN_{eff}^{VR} / dL$ (Jy ^{1.5} sr ⁻¹) (13)	$L^{2.5} dN_{eff}^{V+R} / dL$ (Jy ^{1.5} sr ⁻¹) (14)	$L^{2.5} dN_{eff}^{V-RE} / dL$ (Jy ^{1.5} sr ⁻¹) (15)	$L^{2.5} dN_{eff}^{VRE} / dL$ (Jy ^{1.5} sr ⁻¹) (16)	$L^{2.5} dN_{eff}^{V+RE} / dL$ (Jy ^{1.5} sr ⁻¹) (17)
0.191	0.202	0.215	$0.189^{+0.076}_{-0.056}$	$0.200^{+0.080}_{-0.059}$	$0.212^{+0.085}_{-0.063}$
0.317	0.350	0.379	$0.310^{+0.11}_{-0.082}$	$0.342^{+0.12}_{-0.090}$	$0.371^{+0.13}_{-0.098}$
0.230	0.251	0.270	$0.227^{+0.12}_{-0.084}$	$0.248^{+0.13}_{-0.091}$	$0.266^{+0.14}_{-0.098}$
0.315	0.334	0.353	$0.313^{+0.19}_{-0.12}$	$0.332^{+0.20}_{-0.13}$	$0.350^{+0.21}_{-0.14}$
0.568	0.590	0.613	$0.566^{+0.30}_{-0.21}$	$0.588^{+0.32}_{-0.22}$	$0.611^{+0.33}_{-0.23}$
0.322	0.330	0.340	$0.321^{+0.42}_{-0.21}$	$0.329^{+0.43}_{-0.21}$	$0.339^{+0.45}_{-0.22}$
1.12	1.14	1.17	$1.11^{+0.75}_{-0.48}$	$1.14^{+0.77}_{-0.49}$	$1.17^{+0.79}_{-0.50}$
1.50	1.53	1.56	$1.50^{+1.2}_{-0.72}$	$1.53^{+1.2}_{-0.73}$	$1.56^{+1.2}_{-0.75}$
1.28	1.30	1.32	$1.28^{+1.7}_{-0.83}$	$1.30^{+1.7}_{-0.84}$	$1.33^{+1.7}_{-0.86}$
1.10	1.11	1.13	$1.10^{+2.5}_{-0.91}$	$1.11^{+2.6}_{-0.92}$	$1.13^{+2.6}_{-0.93}$